Mathematical modeling of dermal competence and cellular aggregation effects on feather follicle emergence speed

Maxime Estavoyer, Thomas Lepoutre, Marie Manceau

Mathematical modeling of dermal competence and cellular aggregation effects on feather follicle emergence speed

Maxime Estavoyer[1], Thomas Lepoutre[1], Marie Manceau[2].

[1] Inria, and Université de Lyon, Université Claude Bernard Lyon 1, CNRS UMR 5208, Institut Camille Jordan, F-69603 Villeurbanne, France
[2] Centre for Interdisciplinary Research in Biology, Collège de France, Université PSL, CNRS, INSERM, France

Abstract

During avian morphogenesis, feather follicles generally emerge row by row, in a medio-lateral sequential pattern through a two-stage developmental process. Initially, dermal densification occurs to render the tissue competent. Subsequently, a complex interplay of signaling between dermal cells and proteins leads to the formation of dermal cell aggregates, which initiate feather buds. This study employs a reaction-diffusion-chemotaxis mathematical model to analyze the speeds of these stages and their interactions, to determine the overall emergence speed of feather follicles. Our model enables us to calculate the speed of the competence wave and, through a weakly nonlinear analysis, approximates the emergence speed of follicles within a competence zone. Numerical simulations suggest that when the emergence speed of follicles surpasses the speed of the competence wave, the bud emergence becomes synchronized to the competence wave's speed. Conversely, the formation of follicles does not affect the competence wave. This theoretical and numerical work provides a precise approximation of bud emergence speed in initially naive tissue, highlighting the complex dynamics of feather follicle morphogenesis and the significance of understanding the interplay between dermal competence and cellular aggregation in this process.

1 Introduction

Cutaneous appendages, such as hairs, feathers, and scales, exhibit a multitude of possibilities in terms of arrangement patterns, color variations, shape differences, and timing of appearance among different species. Modeling plays a crucial role in elucidating the underlying mechanisms governing their development and evolution. One influential theoretical framework applied in the field of modeling appendage formation is the reaction-diffusion model, also known as the activator-inhibitor model, developed by Alan Turing [1] (See e.g. [2, 3, 4, 5, 6, 7]). For many species, appendages do not form simultaneously across the entire skin surface, but follow a pattern of sequential development, unfolding in coordinated stages in time and space. This is notably the case for the formation of shark skin denticles [8], the formation of zebrafish scales [9], the formation of bat teeth [3, 10], the formation of feather follicles [7, 11], the formation of corn snake scales [12]. The formation of skin appendages is often correlated with the spatial expansion of the competent tissue region in which the structures can develop. This spatial extension of the competent domain can result from various factors, either dependent on or independent from the morphogens associated with appendage formation. For example, the growth of the dental lamina in bats is directly associated with the formation of molars and premolars [10]. Additionally, the competent zone can also form in the wake of signaling waves, such as Eda waves [7, 12] or NF-κB [9]. Moreover, mechanical phenomena, such as dermal densification, can also render the tissue competent in avian species [11]. In this paper, we focus on the emergence speed of these appendages and choose to concentrate on modeling the spatio-temporal formation of feather follicles.

In birds, feathers are implanted in feather follicles, which are spatially distributed in so-called tracts, or pterylae, separated by glabrous regions. The number, size and extent of tracts vary across the avian phylogeny, but are reproducible within individual species or given families. However, the arrangement of these tracts remains consistent within individual species. Tract variation has been best described in the dorsal region : the dorsal tract may form a thin longitudinal band extending from the neck to the tail (e.g., passerine birds), a thick segment (e.g., ground-dwelling poultry birds), or cover the entire dorsal surface (e.g. ostriches). Strikingly, the local distribution of feather follicles also varies between species, from regular hexagonal patterns where each feather follicle is surrounded by six neighbours to squared meshes or irregular arrangement.

The formation of feather follicles occurs in two distinct phases :

1. *Competent wave :* Early in embryo development, the cells of the dermis begin to organize themselves in different ways depending on their location, which creates structuring spaces. Specifically, the dermis of future appendage areas tends to densify over time, following a medio-lateral wave, playing a crucial role in determining where feathers will emerge [13].
2. *Emergence of feather follicles in the competent area :* Once the dermis is competent, it instructs the overlying epidermis, through local signals, to thicken the epithelial sheet, thereby producing epidermal placodes. These placodes, in turn, send feedback to the dermis, leading to cellular condensation. This process results in the formation of a feather bud from which the feather will emerge.

Note that in the article [7], the authors showed that an ectodysplasin A (Eda) signaling wave cooperates with dermal densification to make the tissue competent. This spatio-temporal

propagation of Eda lowers the cell density threshold required for follicle development by inducing FGF20, which acts as a chemoattractant leading to the aggregation of dermal cells into placodes. However, this signal is neither absolutely necessary nor sufficient for the process of feather follicle formation. In this work, we focus solely on modeling dermal densification as a wave of competence.

In most bird species, the initial appearance of feather primordia is along one or two longitudinal rows in the spinal region. Then, following a medio-lateral wave, new rows of follicles gradually emerge on either side of the initial row, until they reach the boundaries of the appendage fields.

Our aim, through mathematical modeling, is to first compute the respective speeds of these two processes. Then, to investigate the interactions between these stages to determine the speed of emergence of feather follicles during morphogenesis.

In the literature, there are several different reaction-diffusion or reaction-diffusion-chemotaxis models that reproduce regularly spaced dots, closely resembling the feather pattern [11, 14, 15, 16, 17, 18]. Recently, Bailleul et al. explored not only this final hexagonal pattern but also the directional and sequential aspects of feather formation in many bird species [11]. In these articles, the authors defined a mathematical model that intrinsically reproduces this pattern emergence dynamic, as well as the variations between different species. This model combines a system of two reaction-diffusion equations, inspired by the model used in the article by Michon et al. [16], coupled with a classical chemotaxis equation including a logistic proliferation term. More precisely, the model comprises three equations, one for the term n, corresponding to the cell density,

$$\partial_t n = D_n \Delta n - \nabla\cdot(\kappa n \nabla u) + \alpha_n n(1-n), \tag{1}$$

to which we add two reaction-diffusion equations for the species u and v,

$$\partial_t u = D_u \Delta u + \frac{\alpha_u n(1+\omega u^2)}{(\beta_u^2+u^2)(1+v)} - \delta_u u, \tag{2}$$

$$\partial_t v = D_v \Delta v + \alpha_v n u^2 - \delta_v v. \tag{3}$$

We assume that these three species diffuse with a certain diffusion coefficient specific to each one. Concerning the first equation (1), the part in κ is a chemotaxis term, corresponding to a biased diffusion where cells are attracted by the strong gradients of the species u. The cell proliferation term is assumed to be logistic with proliferation rate α_n. This term plays a crucial role in the competence wave, which biologically corresponds to the densification of the dermis. The species u and v correspond, respectively, to the activator and to the inhibitor. Biologically, the exact nature of these species remains uncertain. According to recent work, two candidates stand out : fibroblast growth factor (FGF) for the activator, and BMP (Bone Morphogenetic Protein) for the inhibitor [7]. The system (1)-(3), studied mathematically in the supplementary materials of the article [11], admits, for certain values of parameters, a unique positive equilibrium point denoted as $(1, u_s, v_s)$. This homogeneous state can be Turing unstable, leading to the emergence of patterns representing the arrangement of tracts.

As indicated in the articles [11, 16], this model is mainly chosen for its ability to produce points sequentially. However, the reaction terms of the equations (2) and (3) do not necessarily have a biological interpretation. Therefore, we propose a simplified, but also more general model,

to facilitate the proof of theoretical results. First of all, since the competence wave is unidirectional (medio-lateral), we simplify our problem to a one-dimensional space. Moreover, due to the symmetry around the antero-posterior axis we consider the domain, $\Omega = [0, \ell]$, where ℓ is a positive constant. To simplify the reaction terms of the equations (2) and (3) we employ the following truncation

$$\begin{cases} \partial_t u = D_u \Delta u + n\chi_M(\gamma_u u - \gamma_v v + c_u) - \delta_u u, \\ \partial_t v = D_v \Delta v + n\chi_M(\eta_u u + c_v) - \delta_v v, \end{cases}$$

with $\chi_M(x) = x\mathbf{1}_{0\leq x\leq M}(x) + M\mathbf{1}_{x>M}(x)$, where M is an arbitrary positive constant. To ensure that the truncated model preserves certain essential properties of the original system (1)-(3), we select the constants γ_u, γ_v, and η_u such that the truncated model has the same unique positive equilibrium point $(1, u_s, v_s)$ and the same Jacobian matrix. Therefore, these constants γ_u, γ_v and η_u, are defined as follows,

$$\gamma_u = \frac{2\alpha_u u_s(\omega\beta_u - 1)}{(\beta_u + u_s^2)^2(1 + v_s)}, \quad \gamma_v = \frac{\alpha_u(1 + \omega u_s^2)}{(\beta_u + u_s^2)(1 + v_s)^2}, \qquad \eta_u = 2\alpha_v u_s, \tag{4}$$

concerning the constants c_u and c_v, they are defined by $c_u = -\gamma_u u_s + \gamma_v v_s + \delta_u u_s$ and $c_v = -\eta_u u_s + \delta_v v_s$. This idea of truncation is inspired by the truncation introduced in article [19] ; the aim is to avoid biologically unrealistic interactions. The use of truncation is widely used in the field of pattern emergence modeling, such as for modeling the colors of lizard skin scales [20, 21], the formation of mouse molars [3], the formation of shark skin denticles [8], the color of zebrafish [19], or even the rugae in the mammalian oral palate [22].

Our choice of cut-off function preserves, the positivity of the species u and v and also prevents the explosion by means of the positive constant M for the one and two-dimensional case [23]. If the constant M is assumed to be sufficiently large compared to the amplitudes of the final stationary pattern, the cutoff function will have no impact on the solution of the system. Since the theoretical analysis we perform in this work is only valid for small amplitude perturbations, our calculations reduce to the study of the following model without a cutoff function,

$$\begin{cases} \partial_t n = D_n \Delta n - \nabla\cdot(\kappa n \nabla u) + \alpha_n n\,(1 - n)\,, \\ \partial_t u = D_u \Delta u + n(\gamma_u u - \gamma_v v + c_u) - \delta_u u, \\ \partial_t v = D_v \Delta v + n(\eta_u u + c_v) - \delta_v v. \end{cases} \tag{5}$$

In this article, we are interested in the emergence of patterns, which biologically corresponds to the successive appearance of tracts during morphogenesis. Mathematically, for our model (5), this emergence occurs in two different steps.

1. *Competent wave :* First of all, there is a traveling wave connecting the point $(0, 0, 0)$ (*naive*) to the unique positive equilibrium point $(1, u_s, v_s)$ (*competent*) which corresponds to a densification of the dermis. This step corresponds to the transition between the white area and the green area in Figure 1.
2. *Emergence of feather follicles in the competent area :* Then, in a second step, the linear instability of the point $(1, u_s, v_s)$ leads to the emergence of spatial patterns corresponding to the formation of feather buds. This step corresponds to the transition between the green area and the yellow area in Figure 1.

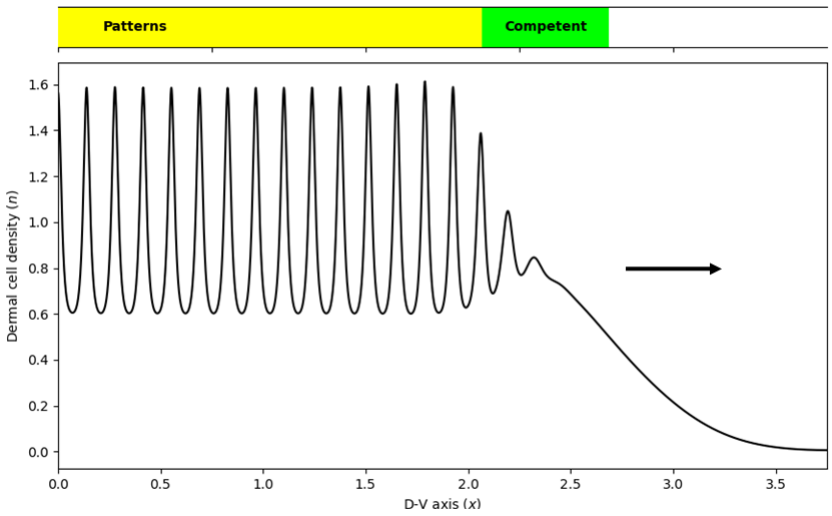

FIGURE 1 – **Emergence of feather follicles.** Snapshot of the density of dermal cells, n, solution of system (5). In the left zone, represented by the yellow color, we observe spatially distributed peaks representing aggregations of dermal cells that are the origin of feather buds. Then, we notice a transition zone, represented by the green color, corresponding to an area where the tissue is competent and where the pattern begins to emerge. Finally, on its right, the naive tissue starts to densify to become competent.

For the model (5), the competence wave is intrinsic to our model. Note that, in many other works, this primary wave is modeled by a wave of competence completely external to the system [17, 24]. More specifically, according to our numerical simulations, this wave of competence closely approximates the solution of the Fisher-KPP scalar equation

$$\partial_t n = D_n \Delta n + \alpha_n n(1-n), \tag{6}$$

corresponding to equation (1) in the case $u = 0$.

This famous equation has been extensively studied [25, 26], and it has been shown that the critical speed is given by $c_{\text{comp}} = 2\sqrt{D_n \alpha_n}$. So, according to our numerical simulations, this competence wave depends solely on dermal densification and the speed is independent of the morphogens u and v.

To study pattern formation in a competent area, we conduct a linear analysis, as well as a weakly nonlinear analysis (WNL) (see for example [27, 28, 29, 30]) to approximate the spatiotemporal evolution of the pattern envelope in a competent area. More precisely, this approximation of the envelope is characterized by the real following Ginzburg-Laudau equation,

$$\partial_T A(X,T) = \nu \partial_{XX} A(X,T) + \sigma A(X,T) - L A^3(X,T). \tag{7}$$

Defined on another scale of time and space $X = \epsilon x$ and $T = \epsilon^2 t$ where the constant $\epsilon > 0$ represents the distance to the Turing bifurcation. When $L > 0$, this weakly nonlinear analysis method proves to be highly relevant close to the bifurcation ($\epsilon \approx 0$) and loses precision as one moves away from this critical bifurcation. The parameters ν, σ, and L depend on the parameters

of the system (5) and are given respectively by the formulas (B.33), (B.34), and (B.35). The study of equation (7) allows us to determine the emergence speed of follicles in a competent dermal tissue, which is given by the formula $c_{\text{nat}} = 2\epsilon\sqrt{\nu\sigma}$, and we will refer to this speed as the *natural speed of patterns*. Unlike the competence wave, the species u and v play an important role in the emergence speed of patterns in a competent area.

Finally, we are interested in the interaction between these two distinct processes, particularly how the competence wave can influence pattern formation and conversely, whether pattern formation can accelerate or slow down the speed of the competence wave. First, when the natural speed of patterns (c_{nat}) is greater than the speed of the competence wave (c_{comp}), pattern emergence will catch up with the competence wave front and "lock" to it without impacting it. In other words, after a certain time, in this case, the speed of the appearance of the patterns is equal to the speed of the primary wave. In the opposite case, the competence wave does not seem to impact the speed of pattern propagation, and consequently, the emergence speed of feather follicles aligns with the the natural speed of patterns. Therefore, the actual speed of feather follicle emergence may either be solely dictated by dermal condensation ($c_{\text{pattern}} = c_{\text{comp}}$) or depend on the complex interactions between dermal cells and the proteins FGF and BMP ($c_{\text{pattern}} \approx c_{\text{nat}}$). The combination of these two cases gives us a very accurate approximation of the speed of appearance of the patterns, given by the following formula

$$c_{\text{pattern}} \approx \min(2\sqrt{\alpha_n D_n}, 2\epsilon\sqrt{\sigma\nu}) = \begin{cases} c_{\text{comp}} = 2\sqrt{\alpha_n D_n}, & \text{if } c_{\text{nat}} > c_{\text{comp}}, \\ c_{\text{nat}} = 2\epsilon\sqrt{\sigma\nu}, & \text{otherwise.} \end{cases} \tag{8}$$

This article is structured as follows. In Section 2, we conduct both linear stability analysis and weakly nonlinear analysis to investigate pattern formation within a competent zone. Additionally, we compare theoretical predictions obtained with numerical simulations. Section 3 is dedicated to the numerical study of the competence wave and its interaction with pattern emergence speed. We perform numerous numerical simulations to propose an approximation of the feather follicle emergence speed in an initially naive tissue.

2 Emergence of feathers in a competent area

2.1 Linear analysis

The linear analysis of the equilibrium $(0, 0, 0)$ can be found in [11], this point is always unstable. In this work, we perform a linear analysis of the positive equilibrium point $(1, u_s, v_s)$. This analysis is presented in Appendix A. More precisely, we are interested in the occurrence of a Turing bifurcation. Specifically, we describe a method to determine the critical value κ_c, such that for all $\kappa > \kappa_c$, the equilibrium point $(1, u_s, v_s)$, which is stable without chemotaxis and diffusion, becomes unstable.

However, the chemotaxis term, κ, is not necessarily required for pattern formation. Indeed, under the assumption $\kappa = 0$, we can find parameter values for which we can observe a Turing instability driven solely by the diffusion coefficients. Nevertheless, chemotaxis greatly facilitates the emergence of patterns. Specifically, an increase in the chemotaxis value, leads to a significant increase in the zone of parameter values where the positive equilibrium point $(1, u_s, v_s)$ exhibits a Turing-type instability [31].

Chemotaxis also plays an important role in the spatial regularity of the stationary pattern. In the article [31], the authors showed that increasing chemotaxis tends to greatly reduce the regularity of the stationary pattern. This loss of regularity can take various forms, such as irregularities in the periodicity of buds, fusion of plumage buds, the appearance of ectopic buds, etc. The regularity of the arrangement of feather follicles in birds varies greatly between species, ranging from low regularity (common ostrich, emu) to nearly perfect regularity (zebra finch, penguin) [32]. However, in bird species with a sequential wave of follicle emergence (e.g. zebra finch, japanese quail, domestic chicken), the arrangement of pterylae is consistently regular. Therefore, in this article, we opt for chemotaxis coefficients close to the critical parameter, that is, $\kappa \gtrsim \kappa_c$, in order to obtain regular stationary patterns.

2.2 Weakly nonlinear analysis (WNL)

The study of linear stability is a useful first step in understanding pattern formation, but it provides only a rough indication of the expected results. Through linear analysis, we determine the conditions on the system parameters required to obtain patterns, and also their frequencies. However, these solutions that grow exponentially according to linear theory do not have physical significance. To predict the amplitude and shape of the pattern near the bifurcation threshold, nonlinear terms must be included in the analysis.

Since this approach allows us to derive explicit quantitative information linking system parameters and pattern amplitude, it can be extremely useful in comparing theoretical system expectations with biological experiments. The key idea of the weakly nonlinear analysis is that, near the bifurcation value, the pattern evolves on a slow time scale so that, using the multiple scales method, one can derive an evolutionary equation for the pattern amplitude. In one-dimensional space domains, a real Ginzburg-Landau type amplitude equation is obtained, which theoretically admits travelling wave type solutions for which the critical speed and the steepness of the wave can be theoretically calculated. Similar work has been conducted for various models related to the system (5), such as nonlinear reaction-diffusion systems [28, 30], with cross-diffusion terms [27, 33, 34, 35, 36], and for volume-filling chemotaxis model [29, 37, 38].

The application of the weakly nonlinear analysis method is detailed in Appendix B. In this section, we summarize the idea of this method. We begin by translating the uniform steady state to the origin, by setting

$$(\tilde{n}, \tilde{u}, \tilde{v}) = (n - 1, u - u_s, v - v_s)\,.$$

To simplify reading, we will omit the tildes and refer to this vector as

$$\mathbf{w} := (\tilde{n}, \tilde{u}, \tilde{v})^T = (n, u, v)^T.$$

Therefore the system (5) can be rewritten as the combination of a linear term and a nonlinear term

$$\partial_t \mathbf{w} = \mathcal{L}\mathbf{w} + \mathcal{B}(\mathbf{w}, \mathbf{w}), \tag{9}$$

where, the linear part $\mathcal{L}$ is defined by

$$\mathcal{L} = J + D^\kappa \partial_{xx}, \quad \text{with} \quad J := \begin{pmatrix} -\alpha_n & 0 & 0 \\ \delta_u u_s & \gamma_u - \delta_u & -\gamma_v \\ \delta_v v_s & \eta_u & -\delta_v \end{pmatrix}, \quad D^\kappa := \begin{pmatrix} D_n & -\kappa & 0 \\ 0 & D_u & 0 \\ 0 & 0 & D_v \end{pmatrix},$$

and the nonlinear part is given by

$$\mathcal{B}(\mathbf{w},\mathbf{w}') := \frac{1}{2}\begin{pmatrix} -\kappa\partial_x(n'\partial_x u + n\partial_x u') - 2\alpha_n n' n \\ \gamma_u(n'u + nu') - \gamma_v(n'v + nv') \\ \eta_u(n'u + un') \end{pmatrix}.$$

To describe the spatial dynamics of the pattern we introduce a new time slow scale as follows

$$t = \mathcal{T}(T_1, T_2, T_3, \ldots), \quad T_i = \epsilon^i t, \quad i = 1, 2, \ldots ,$$

and a new space scale by defining the characteristic length scale of spatial modulation ($X = \epsilon x$), where $\epsilon \ll 1$ represents the distance from the Turing bifurcation point and will be detailed mathematically in the Appendix B. Considering these changes in scale, we have

$$\begin{cases} \partial_x \to \partial_x + \epsilon\partial_X, \\ \partial_{xx} \to \partial_{xx} + 2\epsilon\partial_{xX} + \epsilon^2\partial_{XX}, \\ \partial_t \to \epsilon\partial_{T_1} + \epsilon^2\partial_{T_2} + \epsilon^3\partial_{T_3} + \cdots . \end{cases} \tag{10}$$

Moreover, we expand κ and $\mathbf{w}$ in the small parameter as

$$\begin{cases} \kappa = \kappa_c + \epsilon\kappa_1 + \epsilon^2\kappa_2 + \epsilon^3\kappa_3 + \ldots , \\ \mathbf{w} = \epsilon\mathbf{w}_1 + \epsilon^2\mathbf{w}_2 + \epsilon^3\mathbf{w}_3 + \ldots . \end{cases} \tag{11}$$

where $\mathbf{w}_i = (n_i, u_i, v_i)^T$. Using the relations (10) and (11), we expand the linear part and the nonlinear part in terms of powers of ϵ, which yields for fixed f

$$\mathcal{L}(f) = \mathcal{L}^0(f) + \epsilon\mathcal{L}^1(f) + \epsilon^2\mathcal{L}^2(f) + \epsilon^3\mathcal{L}^3(f) + \cdots , \tag{12}$$

and,

$$\mathcal{B}(f,g) = \mathcal{B}^0(f,g) + \epsilon\mathcal{B}^1(f,g) + \epsilon^2\mathcal{B}^2(f,g) + \cdots . \tag{13}$$

where $(\mathcal{L}^i)_i$ and $(\mathcal{B}^i)_i$ are operators specified in Appendix B. We expand each term of equation (9) to identify the terms of each power of ϵ, it gives,

$$\begin{array}{rcccccc} \partial_t\mathbf{w} = & 0 & +\epsilon.0 & +\epsilon^2\partial_{T_1}\mathbf{w}_1 & +\epsilon^3(\partial_{T_1}\mathbf{w}_2 + \partial_{T_2}\mathbf{w}_1) & +O(\epsilon^3), \\ \mathcal{L}(\mathbf{w}) = & 0 & +\epsilon\mathcal{L}^0(\mathbf{w}_1) & +\epsilon^2\left(\mathcal{L}^0(\mathbf{w}_2) + \mathcal{L}^1(\mathbf{w}_1)\right) & +\epsilon^3\left(\mathcal{L}^0(\mathbf{w}_3) + \mathcal{L}^1(\mathbf{w}_2) + \mathcal{L}^2(\mathbf{w}_1)\right) & +O(\epsilon^3), \\ \mathcal{B}(\mathbf{w},\mathbf{w}) = & 0 & +\epsilon.0 & +\epsilon^2\mathcal{B}^0(\mathbf{w}_1,\mathbf{w}_1) & +\epsilon^3\left(2\mathcal{B}^0(\mathbf{w}_1,\mathbf{w}_2) + \mathcal{B}^1(\mathbf{w}_1,\mathbf{w}_1)\right) & +O(\epsilon^3). \end{array}$$

Therefore, to ensure a matching up to order 3, one needs to solve for $\mathbf{w}_{1,2,3}$ the system

$$0 = \mathcal{L}^0(\mathbf{w}_1) + 0, \tag{14}$$

$$\partial_{T_1}\mathbf{w}_1 = \left(\mathcal{L}^0(\mathbf{w}_2) + \mathcal{L}^1(\mathbf{w}_1)\right) + \mathcal{B}^0(\mathbf{w}_1,\mathbf{w}_1), \tag{15}$$

$$(\partial_{T_1}\mathbf{w}_2 + \partial_{T_2}\mathbf{w}_1) = \left(\mathcal{L}^0(\mathbf{w}_3) + \mathcal{L}^1(\mathbf{w}_2) + \mathcal{L}^2(\mathbf{w}_1)\right) + \left(2\mathcal{B}^0(\mathbf{w}_1,\mathbf{w}_2) + \mathcal{B}^1(\mathbf{w}_1,\mathbf{w}_1)\right). \tag{16}$$

At $O(\epsilon)$ we recover the linear problem $\mathcal{L}^0(\mathbf{w}_1) = 0$, whose solution satisfying the Neumann boundary conditions is

$$\mathbf{w}_1 = A(T_1, T_2, \ldots; X)\rho\cos(k_c x), \tag{17}$$

where k_c corresponds to the first and unique unstable mode and $A(T_1, T_2, \ldots; X)$ is the spatial amplitude of the pattern. The vector ρ is derived in the appendix B and given by the relation (B.25).

At $O(\epsilon^2)$, we combine formula (17) and the Fredholm alternative to determine the following equalities.

$$T_1 = 0, \qquad \kappa_1 = 0,$$

as well as the definition of the vector $\mathbf{w}_2$, defined as follows

$$\mathbf{w}_2 = A^2\mathbf{w}_{20} + A^2\mathbf{w}_{22}\cos(2k_c x) + \frac{\partial A}{\partial X}\mathbf{w}_{21}\sin(k_c x), \tag{18}$$

where $\mathbf{w}_{2i}$, $i = 0, 1, 2$, are the solutions of the system (B.32).

Finally, at $O(\epsilon^3)$, using the solvability condition and equality (18), one finds the following real Ginzburg-Landau equation for the amplitude A,

$$\partial_{T_2} A = \nu\partial_{XX} A + \sigma A - LA^3.$$

where the parameters ν, σ and L are given by the equations (B.33), (B.34) and (B.35) respectively. Since the growth rate coefficient σ is always positive, the dynamics of the real Ginzburg-Landau equation (7) can be divided into two different cases depending on the sign of the constant L : the supercritical case, when L is positive, and the subcritical case, when L is negative.

When $L < 0$ the real Ginzburg-Landau equation (7) is not able to capture the amplitude of the pattern. Therefore, it's necessary to push the weakly nonlinear expansion up to order five. However, in this case, the actual expected amplitude, ϵA, is of order $O(1)$ [35]. Therefore, the approximation proposed by the weakly nonlinear analysis generally does not match the asymptotic solutions. This lack of precision has been observed in many articles (e.g., [27, 38, 35]). Moreover when we add the slow modulation in space, the equation obtained at order 5 is very complex [37] and, to our knowledge, there is no work concerning the theoretical existence of a positive traveling wave for this kind of equation. Therefore, in the following we will only be interested in the case where L is positive.

Conclusion of the weakly nonlinear analysis To sum up, the asymptotic expression for the spatial pattern of (5), when $L > 0$, is given by

$$\begin{pmatrix} n \\ u \\ v \end{pmatrix} = \begin{pmatrix} 1 \\ u_s \\ v_s \end{pmatrix} + \epsilon A(\epsilon x, \epsilon^2 t)\rho\cos(k_c x) + O(\epsilon^2), \tag{19}$$

where the amplitude A is the solution of the Eq. (7).

Expected stationary patterns. The Eq. (7) admits two nonnegatives points equilibrium, the unstable point $A = 0$ and the stable positive point $A_\infty := \sqrt{\sigma/L}$. This equilibrium point is globally asymptotically stable and we thus have $\lim_{T_2 \to +\infty} A(X, T_2) = A_\infty$ for all X. Therefore the

weakly nonlinear analysis, at order 3, gives us the following approximation for the final stationary pattern

$$\begin{pmatrix} n(x) \\ u(x) \\ v(x) \end{pmatrix} = \begin{pmatrix} 1 \\ u_s \\ v_s \end{pmatrix} + \epsilon A_\infty \rho \cos(k_c x) + \epsilon^2 A_\infty^2 \left(\mathbf{w}_{20} + \mathbf{w}_{22} \cos(2k_c x)\right) + O(\epsilon^3). \tag{20}$$

Expected speed of pattern spread. It is well known from the literature that, for L positive, the equation (7) admits traveling wave type solutions connecting 0 to A_∞. The associated critical speed, denoted $c^\star_{\text{WNL}}$, is given by $c^\star_{\text{WNL}} := 2\sqrt{\nu\sigma}$ [39]. For an initial condition with finite initial support, the selected speed corresponds to the critical speed [26]. For $c = c^\star_{\text{WNL}}$ the steepness of the front, denoted $\mu^\star$, is given by, $\mu^\star = \sqrt{\sigma/\nu}$.

Note that the speed $c^\star_{\text{WNL}}$ correspond to the pattern emergence speed in the slow scale. To obtain the emergence speed of follicles in the correct scale, we must multiply it by ϵ, resulting in,

$$c_{\text{nat}} = \epsilon c^\star_{\text{WNL}} = 2\epsilon\sqrt{\nu\sigma}.$$

2.3 Expected stationary patterns

When ϵ is small enough, we can see in the figure 2A that the approximation (20) predicted by the weakly nonlinear analysis is very accurate. The dashed red line corresponding to the approximation (20), while the black line corresponds to a solution of the equation (5), obtained using a numerical simulation. Similarly, for $\epsilon = 0.3$, we notice that the analysis remains quite close to the numerical solution (Fig. 2B below). We have also computed the bifurcation diagram of model (5), shown in Figure 2C, using the `Matlab` package `pde2path` [40, 41]. The code is adapted from the codes presented in the tutorial [42]. In Figure 2C we also plot, in red, the prediction given by weakly nonlinear analysis (20). The bifurcation diagram validates both the numerical simulations in Figure 2A-B and the accuracy of the weakly nonlinear analysis.

2.4 Expected speed of pattern spread in a competent area

In Figure 3 we compare over time the result of the weakly nonlinear analysis (dashed red line) with the numerical solution of the system (5) (black line) for a small ϵ ($\epsilon = 0.05$). The initial amplitude chosen is given by $A_0(X) = A_\infty.\mathbf{1}_{|X|\leq K}$ with K some positive constant. For this initial data, it is known that the speed of the wave corresponds to the critical speed $c^\star_{\text{WNL}}$ [26]. The approximation obtained by the weakly nonlinear analysis closely matches the numerical results.

In Figure 14, we again compare the numerical solution of the system (5) (black line) with the prediction of the weakly nonlinear analysis (blue dashed line), but this time for $\epsilon = 0.2$. As expected, the analysis loses precision, however the approximation of the speed of pattern emergence is still very precise. More particularly we notice an overshoot phenomenon, when the inhomogeneity appears it tends to increase very quickly up to a certain maximum then will decrease towards a stationary amplitude quite close to the amplitude predicted by the weakly nonlinear analysis, ϵA_∞. In other words, far enough from the Turing bifurcation, the amplitude wavefront becomes non-monotonic.

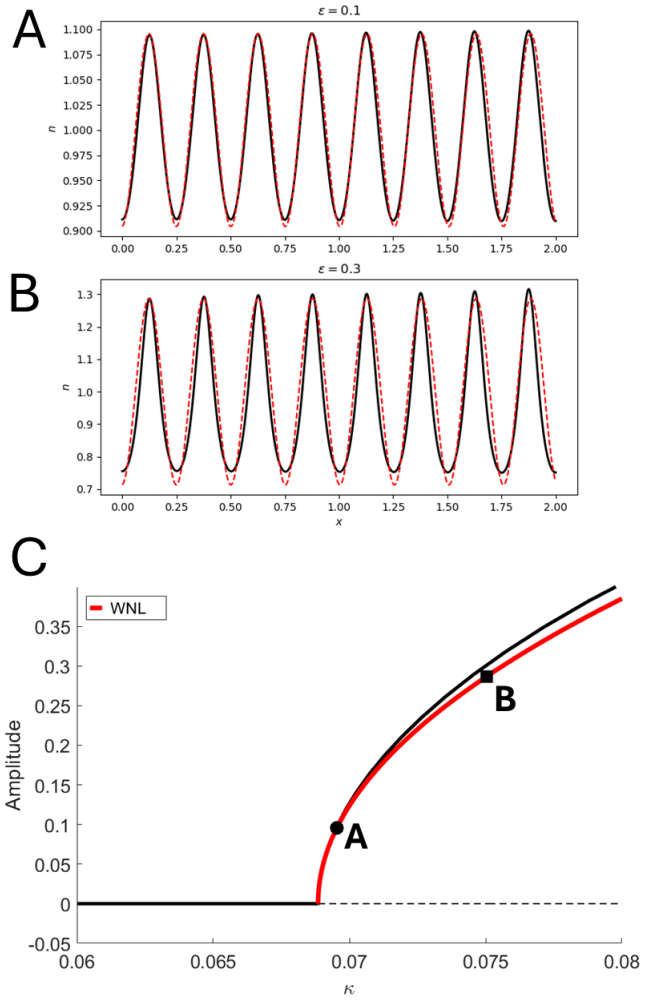

FIGURE 2 – **Expected stationary patterns.** *A-B.* Comparison between the weakly nonlinear approximation (20) (red dashed line) and the numerical solution of (5) (black solid line). *A.* $\epsilon = 0.1$. *B.* $\epsilon = 0.3$. *C.* Comparison of the bifurcation diagram obtained with `pde2path` (black curve) and the prediction obtained using the weakly nonlinear analysis (20) (red curve). The dotted line corresponds to the equilibrium point becoming unstable following a super-critical Turing bifurcation. The black circle corresponds to $\epsilon = 0.1$ (A.) and the black square to $\epsilon = 0.3$ (B.). Parameter values are : $D_n = 0.1$, $D_u = 6\text{e} - 3$, $Dv = 0.13$, $\gamma_u = 15.539$, $\gamma_v = 0.01$, $\eta_u = 3931$, $c_u = 2.9672$, $c_v = -1104$ and $\alpha_n = 0.5$.

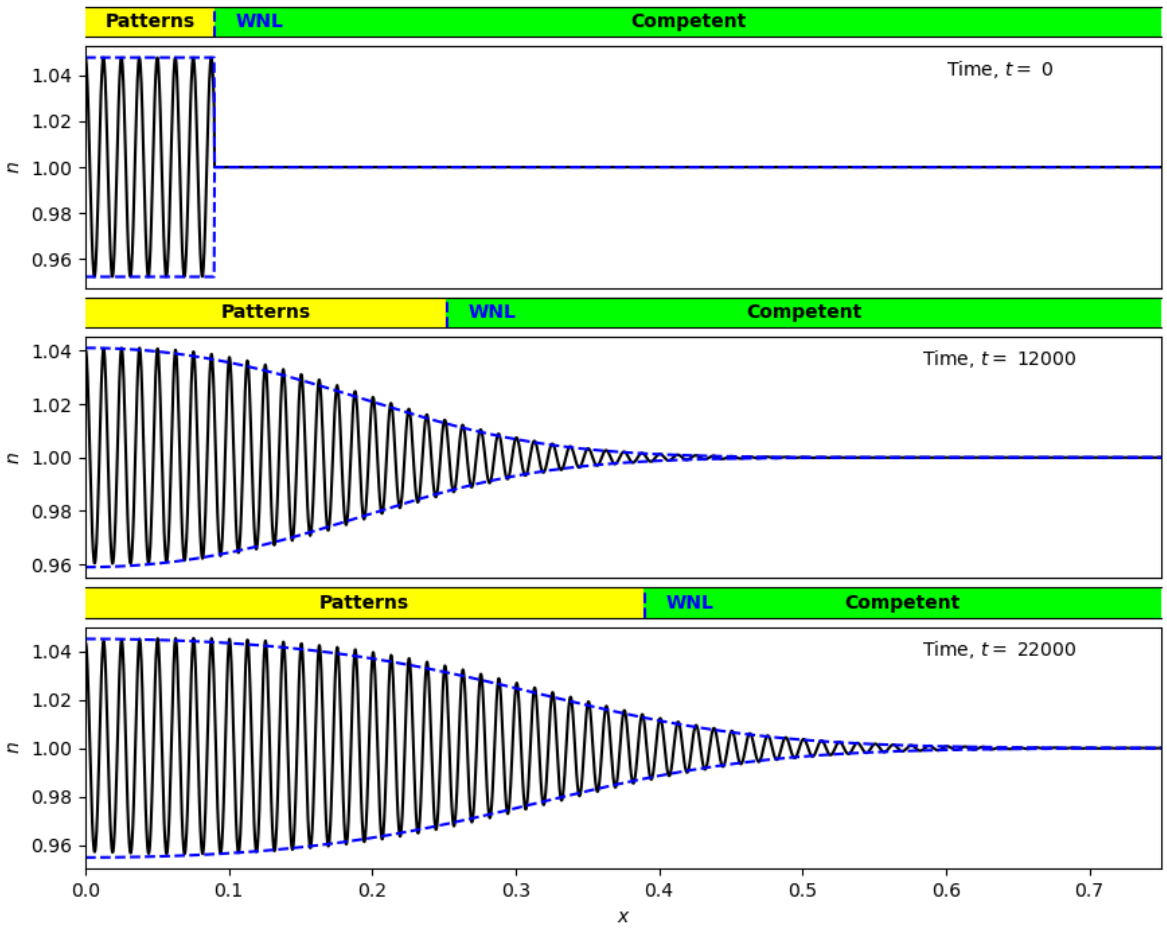

FIGURE 3 – **Comparison between the solution of the equation** (7) **(blue dashed line) and the numerical solution of** (5) **(black solid line) at different times.** The panels above the figures respectively represent the competent zone (green), the zone where patterns are present (yellow), and the prediction of the weakly nonlinear analysis (blue dashed line). Parameter values are given by : $D_n = 7\mathrm{e}-5$, $D_u = 6\mathrm{e}-3$, $Dv = 0.13$, $\gamma_u = 14.5389$, $\gamma_v = 0.099932$, $\eta_u = 3931$, $c_u = 2.9672$, $c_v = -1104$, $\alpha_n = 0.001$ and $\epsilon = 0.05$.

2.5 Influence of parameter values on pattern formation

In this section we are interested in the impact of the different parameters on the values of interest of our problem which are : the final stationary amplitude of the pattern A_∞, the critical speed of the emergence of the patterns $c^\star_{\mathrm{WNL}}$ as well as the steepness of the front $\mu^\star$. The variation of a parameter affects these values in two ways, firstly it directly influences the variables σ, L and ν defined explicitly in terms of the system parameters (5) ; moreover, the variation of a parameter, also impacts critical value κ_c and the eigenvalues. We only focus in the impact of the system parameters (5) on the variables σ, L and ν. Therefore for each variation of parameter values, we recalculate κ_c again.

Influence of parameters on critical speed, $c^\star_{\mathrm{WNL}}$, and on the steepness of the amplitude front, $\mu^\star$. The critical speed $c^\star_{\mathrm{WNL}} := 2\sqrt{\sigma\nu}$, of the traveling wave type solutions for the equation (7), obtained following the analysis weakly nonlinear, is dependent on the parameters σ and ν, themselves dependent on the parameters of the system (5). In the figure 11, we are interested in the influence of the different parameters of the system (5) on the critical speed $c^\star_{\mathrm{WNL}}$. The increase of the diffusion coefficient D_n leads to a faster critical speed, this growth is initially exponential and then goes almost to zero. The influence of the coefficients D_u and D_v is ambivalent. Indeed, the critical speed increases when the diffusion coefficient D_u also increases. Conversely, the speed decreases as the coefficient D_v increases. The impact of the α_n parameter on the critical speed $c^\star_{\mathrm{WNL}}$ is very small compared to the strong variations of the parameter. The influence of the parameters γ_u, γ_v and η_u is quite similar : the speed of emergence of the patterns increases as the parameter value increases. Concerning the parameter δ_v, the speed $c^\star_{\mathrm{WNL}}$ decreases linearly. Finally, for the parameter γ_u, it has the opposite effect of its counterpart, γ_v.

A similar work for the steepness of the propagation front is illustrated in Figure 12. For the parameters D_v, δ_u, δ_v, γ_u, γ_v and η_u, their influence on the steepness is similar to their influence on the speed of the wave, $c^\star_{\mathrm{WNL}}$. Conversely, the variation of the parameter D_n has the opposite effect than its impact on the critical speed. For the proliferation parameter α_n, we notice that the front steepness is proportional to it. Concerning the parameter D_v, it is more difficult to draw conclusions, when D_v increases the steepness is initially increased then it decreases.

Influence of parameters on stationary amplitude, A_∞. In the same way, we study the influence of the parameters on the final amplitude of the spatial patterns. In the case $L > 0$, the final amplitude is given by $A_\infty = \sqrt{\sigma/L}$, with σ and L defined respectively by (B.34) and (B.35). We illustrate in figure 13, the impact of each parameter of the system (5) on the value of A_∞.

For this work, we have chosen to study the parameters γ_u, γ_v and η_u directly. By definition (1) we can also deduce the impact of the parameters used in the system (1)-(3) defined in the article [11]. For example, a variation of the α_u parameter would impact both the γ_u term and the γ_v term and thus have a particular influence on the critical speed or on the steepness. However, as stated before, the system (1)-(3) is not based on a biological interpretation, so we only focus on our simplified model (5), which is, in a certain sense, more general.

3 Competence wave followed by the emergence of feather follicles

In the previous section, we showed that weakly nonlinear analysis, sufficiently close enough to the bifurcation, accurately predicts the behavior of solutions of system (5) when initialized near the unstable equilibrium point $(1, u_s, v_s)$, that is, when the tissue is assumed to be already competent. In this section, we focus on the impact of having an initially mostly naive tissue, with low or even null quantity of cells and proteins. In other words, mathematically, we study the impact of taking initial data with finite support on the speed of pattern emergence. More precisely, we are interested in a two-step process, first a wave connecting $(0, 0, 0)$ to $(1, u_s, v_s)$, corresponding to a *wave of competence*, and then, in the wake of this primary wave, the emergence of patterns around this unstable point, corresponding to *the emergence of feather follicles*.

3.1 Competence wave

First of all, we are interested in the competence wave. Numerically, we notice that the system (5) numerically admits traveling wave solutions connecting the null point to the equilibrium point $(1, u_s, v_s)$. First we derive the linear spreading speed of the system (5). In our case, the linearization decouples the system and the linearized system shares the same linear part as the Fisher-KPP scalar equation,

$$\partial_t n = D_n \Delta n + \alpha_n n(1 - n).$$

For this equation, it is known that traveling wave type solutions have the critical speed $c_{\text{comp}} := 2\sqrt{D_n \alpha_n}$, which therefore corresponds to the linear spreading speed of the system (5). Even if the linear speed is often a good prediction of the nonlinear speed, theoretically it can be different [43]. Numerically, for the different parameter values tested, the nonlinear speed seems always equal to the linear spreading speed, and this, for the different cases described just below. However, due to the large number of parameters and the difficulty of accurately approximating speed of a traveling wave, it is possible that the nonlinear speed may differ from the linear speed for some untested parameter areas. When nonlinear speed corresponds to linear speed, the traveling wave is caused by the spread of cells and more particularly by the diffusion term and by the proliferation term in the first equation of the system (5). Conversely, chemotaxis has not impact on the speed of competence wave.

The equilibrium point $(1, u_s, v_s)$ can be linearly stable or unstable. In the case where this equilibrium point does not admit Turing instability, we notice that this system numerically admits a traveling wave type solution with a speed and a front very close to the solution of the Fisher-KPP equation (6). This result is represented in the figure 4 in which the black lines correspond to the numerical solution n of the system (5) at differents times and the red line represents the numerical solution of the associated Fisher-KPP equation (6). For both simulations we take the same initial condition which is represented in the top panel. For this type of initial data, the selected speed of the traveling wave solution of the associated Fisher-KPP equation (6), corresponds the critical Fisher-KPP speed [26].

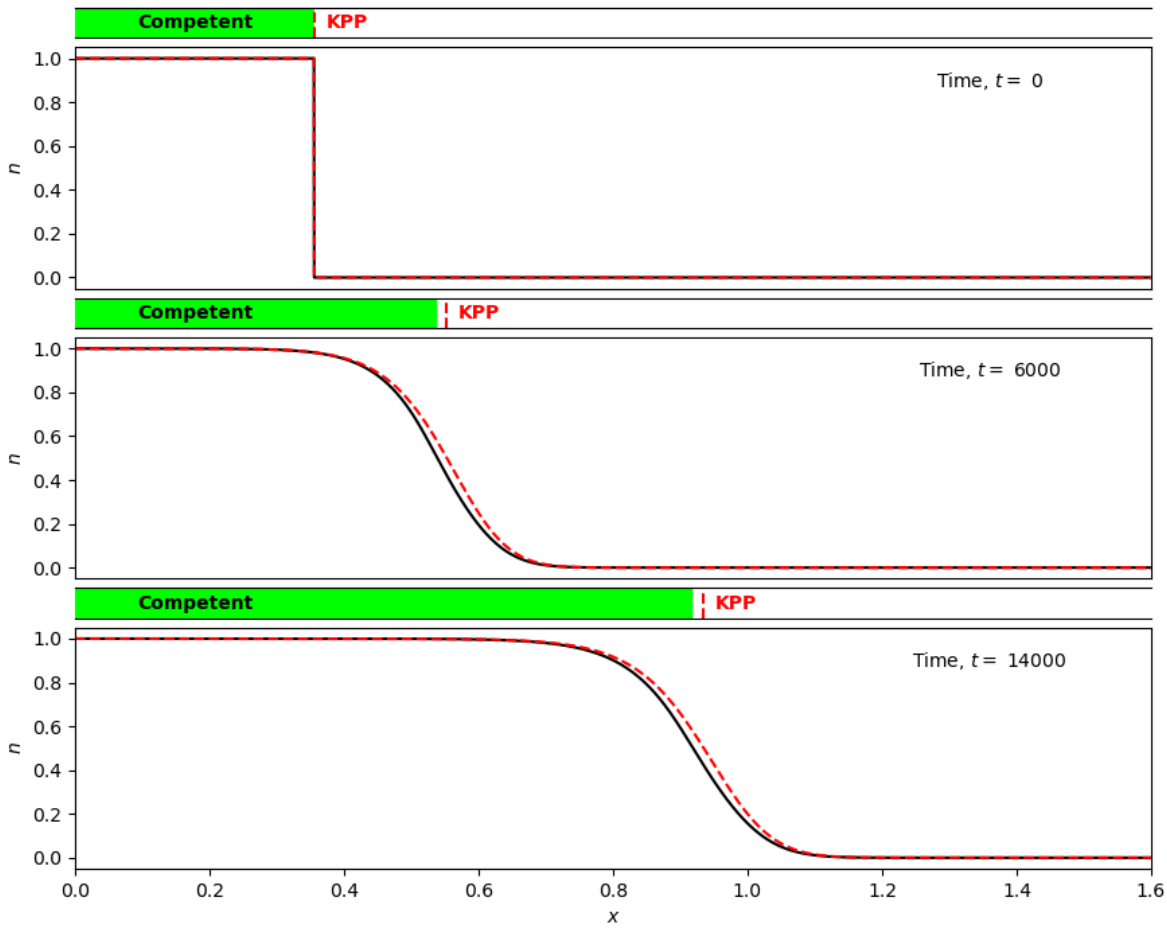

FIGURE 4 – **Competence wave.** Numerical simulation of the system (5) (black line) and of the associated Fisher-KPP equation (6) (red dashed line) when the equilibrium point $(1, u_s, v_s)$ is stable. The panels above the figures represent the competent zone (in green) and the propagation of the solution to the Fisher-KPP equation (red dashed line). Parameter values are given by : $D_n = 7\text{e}-5$, $D_u = 6\text{e}-3$, $Dv = 0.13$, $\gamma_u = 14.5389$, $\gamma_v = 0.099932$, $\eta_u = 3931$, $c_u = 2.9672$, $c_v = -1104$, $\alpha_n = 0.001$ and $\kappa = 4.84\text{e}-5 < \kappa_c$.

3.2 Competence wave and the natural speed of patterns

When the point $(1, u_s, v_s)$ is unstable, the solutions become more complex as a heterogenous pattern now forms in the wake of the competence wave. In this case, the space is structured into three distinct zones. The first zone corresponds to an area where feather buds are well established, mathematically it corresponds to a zone where patterns are present and well-defined. The second zone is an intermediate area, corresponding both to tissue that has just become competent and to tissue where aggregates are beginning to form. As we shall see, this zone may be small in size or even non-existent. The third zone corresponds to naive tissue, in which dermal cells are sparse, this zone is mathematically defined by $\{x : \ n(t,x) < 1/2, \ x \in \Omega\}$. Assuming that these two processes occur independently, we know that the speed of the first stage, the competence wave (transition between naive and competent tissue), is given by c_{comp}. The second stage, corresponding to the natural emergence of patterns in a competent zone (transition between the "Patterns" zone and the "Competent" zone), occurs at a speed c_{nat}, predicted by weakly nonlinear analysis. In this case, there are two possible scenarios : either the speed c_{comp} is greater than the speed c_{nat}, or the opposite. We discuss these two possibilities below.

Competence wave slower than the natural speed of patterns. When the speed predicted by the weakly nonlinear analysis, denoted c_{nat}, is, greater than the speed c_{comp}, the spread of the patterns will "lock" with the primary competence wave. Indeed, as we can see in the figure 6, the speed of pattern emergence of the numerical solution of the system (5) (curve in black), will correspond to the speed of the primary wave connecting $n = 0$ to $n = 1$, itself very close to the speed of the solution of the associated Fisher-KPP equation (6) represented in red dashed line in the figure 6. Consequently, the fact that the natural speed is greater will not affect the speed of the competence wave. In this case, the competence zone will remain constant and small in size throughout the simulation. This phenomenon is also illustrated in the top kymograph of Figure 7. The gray color intensity represents the density of cells, n. The dashed red line corresponds to the theoretical speed of the Fisher-KPP equation. In this figure, we notice that the pattern emergence perfectly aligns with this speed. Numerically, we can conclude that, in this case, $c_{\text{pattern}} \approx c_{\text{comp}} < c_{\text{nat}}$. We tried for several sets of parameter values and the behavior was always similar.

We have also studied a system similar to the system (5), where dermal cell proliferation is now given by the growth term $\alpha_n n(1-n)(1+an)$, with $a \in [-1, +\infty[$. The equation associated with this system sharing the same travelling wave of competence is given by the following scalar equation

$$\partial_t n = D_n \Delta n + \alpha_n n(1-n)(1+an). \tag{21}$$

This equation has also been extensively studied and the critical speed has been derived explicitly. For this slightly modified system, we notice again the "locking" phenomenon for the different sets of parameters tested. Note that we have tested for different values a, notably for large a for which the associated Fisher-KPP equation, called also Nagumo equation, admits pushed fronts [39].

Competence wave faster than the natural speed of patterns. Concerning the opposite case, i.e. when the primary wave is faster than the speed of emergence of the patterns, the result is quite different. Indeed, as we can see in the figure 6, the speed of appearance of the

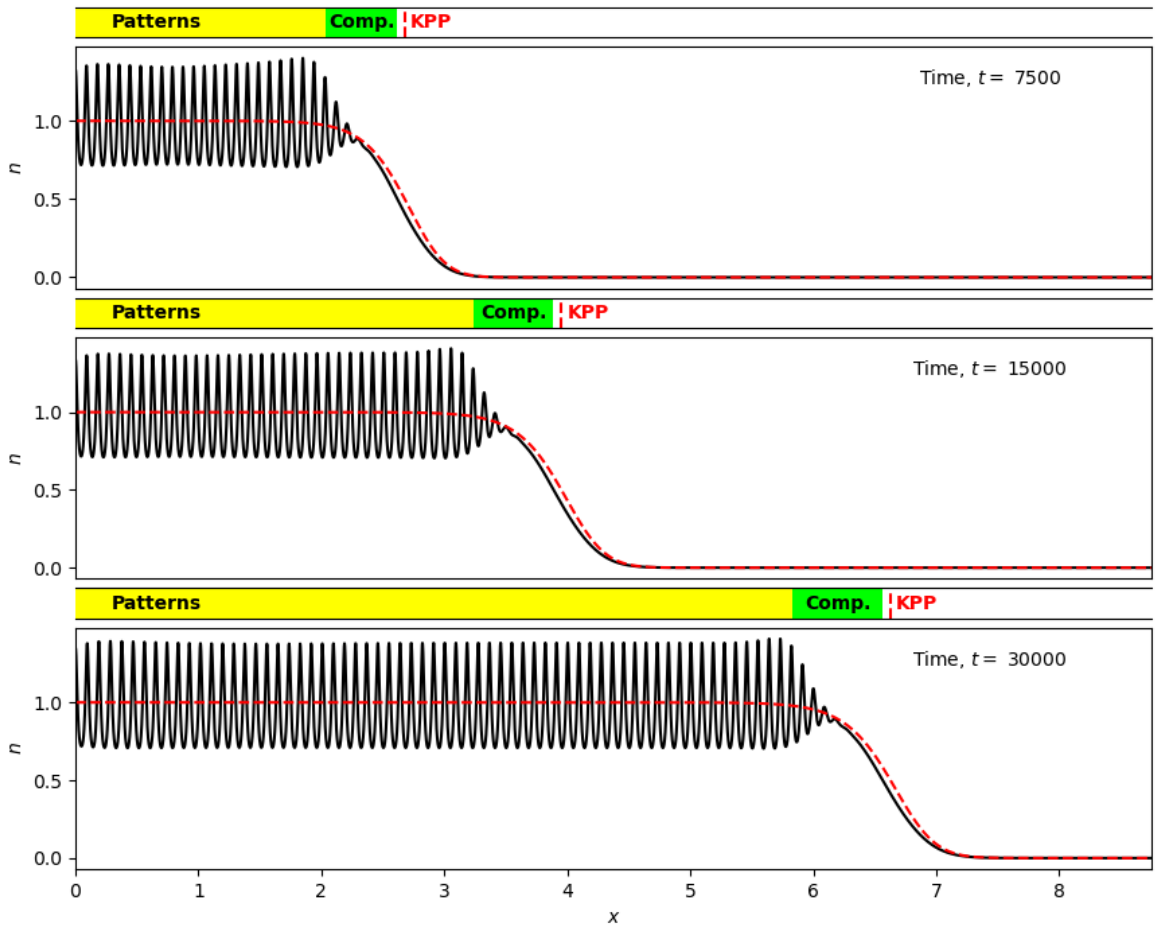

FIGURE 5 – **Competence wave slower than the natural speed of patterns.** Numerical simulation of the system (5) (black line) and of the associated model (6) (red dashed line) when the point $(1, u_s, v_s)$ is unstable and when $c_{\text{comp}} < c_{\text{nat}}$. The panels above the figures show the patterns/competence areas (green/yellow) and the propagation of the solution to the Fisher-KPP equation (red dotted line). Parameter values are given by : $\epsilon = 0.3$, $D_n = 7\text{e}-5$, $D_u = 6\text{e}-3$, $D_v = 0.13$, $\gamma_u = 14.5389$, $\gamma_v = 0.099932$, $\eta_u = 3931$, $c_u = 2.9672$, $c_v = -1104$, $\alpha_n = 0.001$.

patterns will be almost similar to that predicted by the weakly nonlinear analysis. The black curve corresponds to the numerical simulation of the system (5), for three different times. The curves in blue correspond to the theoretical envelope calculated using the equation (7) given by the weakly nonlinear analysis. In this simulation, the choice of the initial condition can create a certain delay between the amplitude predicted by the weakly nonlinear analysis and the actual amplitude of the patterns. Therefore, we illustrate the solution with a certain delay, similar for the 3 sub-figures, $A(t_i + T)$, with $T = 9000$. The red curve corresponds to the numerical solution of the Fisher-KPP equation associated with our problem. Again we notice that the first wave connecting $(0, 0, 0)$ to $(1, u_s, v_s)$ is very close to the wave of the Fisher-KPP equation associated with our system, and we also notice that the weakly nonlinear analysis describes very precisely the installation of patterns in the wake of this primary wave. In this scenario, since the competence speed is faster, the competent zone will continue to grow, mathematically corresponding to the formation of a "terrace". Furthermore, this competence wave has absolutely no impact on the pattern installation speed. These conclusions are also confirmed in the lower kymograph of Figure 7.

Influence of parameter values α_n and D_n on the speed of feather follicle emergence. The parameters α_n and D_n are crucial as they influence both critical speeds c_{comp} and c_{nat}. In Figure 8, we plot the influence of parameters value D_n and α_n on the two theoretical critical speeds. The blue curve corresponds to the natural speed, c_{nat}, and the red curve corresponds to the competence wave speed, c_{comp}. The black crosses correspond to the actual speed of pattern installation from the numerical solution of system (5). To determine the pattern installation speed, we first identify local maxima associated with the patterns, then interpolate them to obtain an approximate envelope of the patterns. Once this envelope is obtained, we use a scout & spot algorithm to determine its speed over time. Instead of directly comparing these approximate values to theoretical speeds, we also illustrate, with colored points, the approximate numerical speeds using a similar algorithm, of travelling wave solutions of the Fisher-KPP equation (6) (Red points) and of the envelope equation (7) (Blue points). We take care to use the same discretization and simulation time to ensure comparable results. In Figure 8, we observe the two previously mentioned possibilities. When the natural speed is faster, the competence wave governs the speed of follicle installation (Bold red curve). Conversely, when the competence wave speed is faster, the speed of follicle installation corresponds to the natural emergence speed of the pattern (Bold blue curve).

4 Conclusion

In conclusion, based on our theoretical and numerical work on a general model inspired by the article [11], we propose an approximation of the speed of emergence of feather follicles. Specifically, two possibilities arise. If the competence wave is slow compared to the natural emergence speed of feather buds, these buds will invade the competent zone and synchronize with the competence wave. Consequently, in this scenario, the speed is solely determined by the dermal densification, which mathematically corresponds to the speed $c_{\text{comp}} = 2\sqrt{D_n \alpha_n}$, with D_n being the diffusion coefficient and α_n the dermal cell proliferation rate. Conversely, when

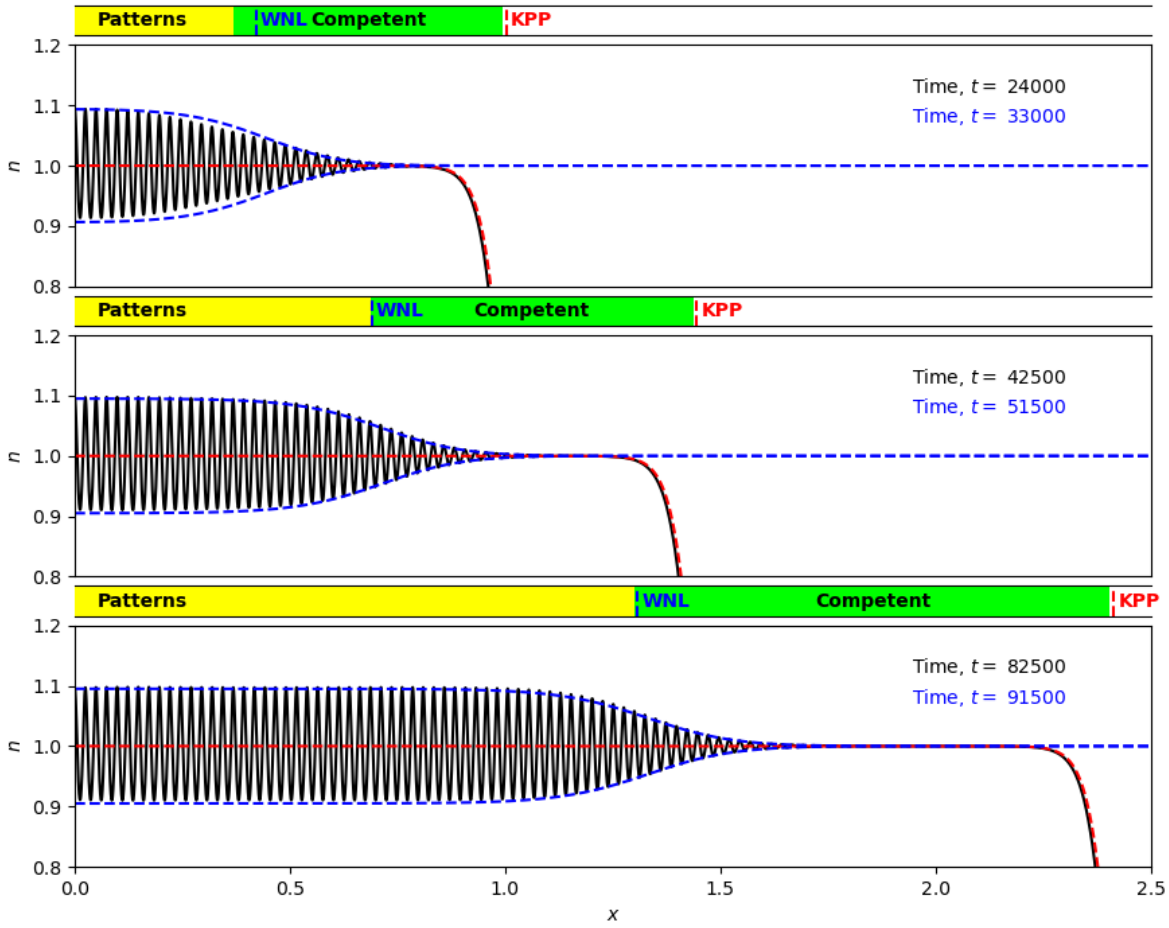

FIGURE 6 – **Competence wave faster than the natural speed of patterns.** Numerical simulation of the system (5) (black line) and of the associated model (6) (red dashed line) when the point $(1, u_s, v_s)$ is unstable and when $c_{\text{comp}} \geq c_{\text{nat}}$. The blue curve corresponds to the approximation (19) obtained using the weakly nonlinear analysis, with a similar time delay for the 3 figures. The panels above the figures show the patterns/competence areas (green/yellow), the propagation of the solution to the Fisher-KPP equation (red dotted line) and the propagation of the approximate envelope (blue dotted line). Parameter values are given by : $D_n = 7\text{e}-5$, $D_u = 6\text{e}-3$, $D_v = 0.13$, $\gamma_u = 14.5389$, $\gamma_v = 0.099932$, $\eta_u = 3931$, $c_u = 2.9672$, $c_v = -1104$, $\alpha_n = 0.001$ and $\kappa = 4.9\text{e}-5$.

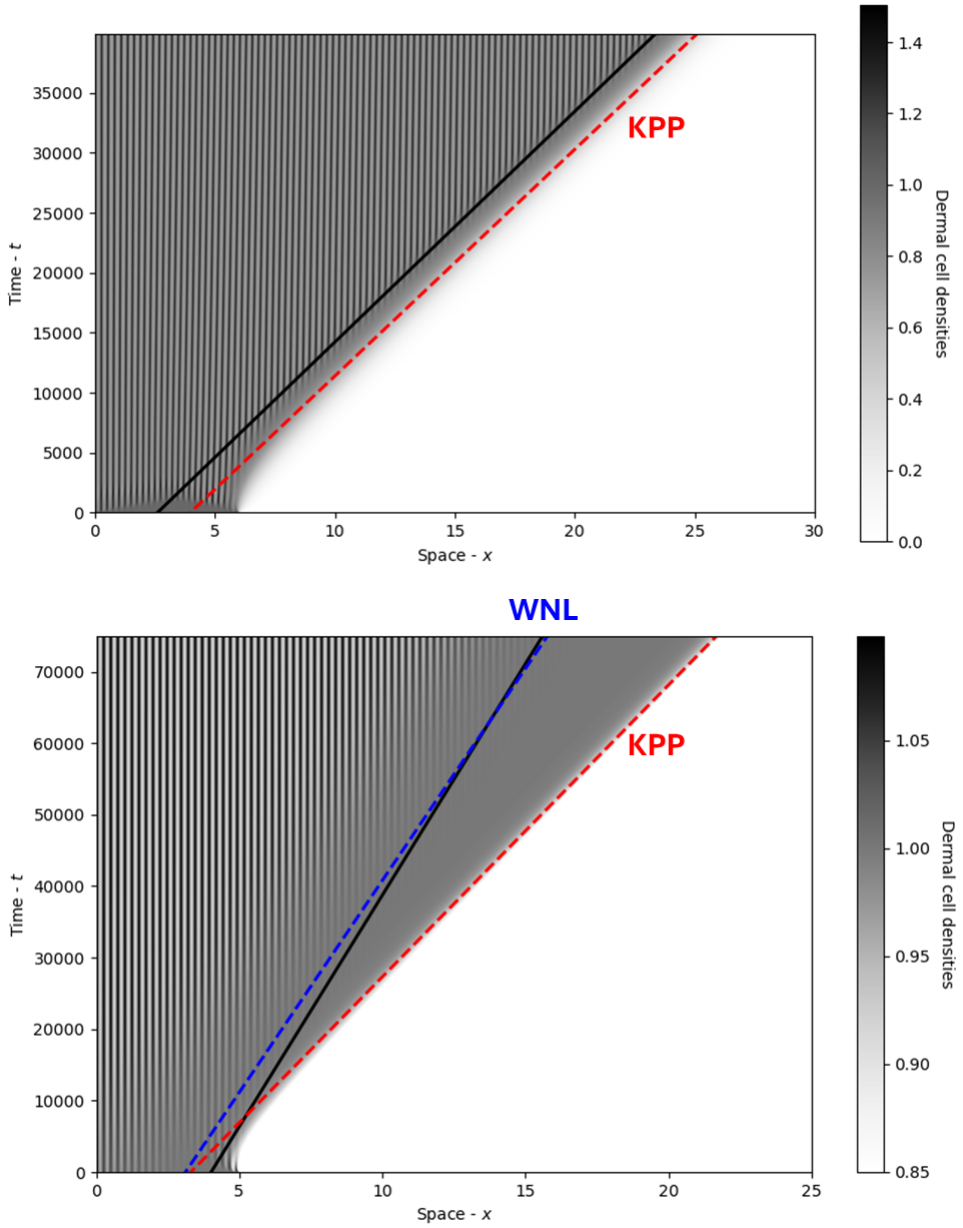

FIGURE 7 – **Density plot of n of the numerical solution to the system (5) when $c_{\mathbf{nat}} > c_{\mathbf{comp}}$ (*Top*) and when $c_{\mathbf{nat}} < c_{\mathbf{comp}}$ (*Bottom*).** The dashed red and blue lines correspond respectively to the theoretical speed c_{comp} and c_{nat}. The parameter values are similar to those in Figure 5 and 6 respectively.

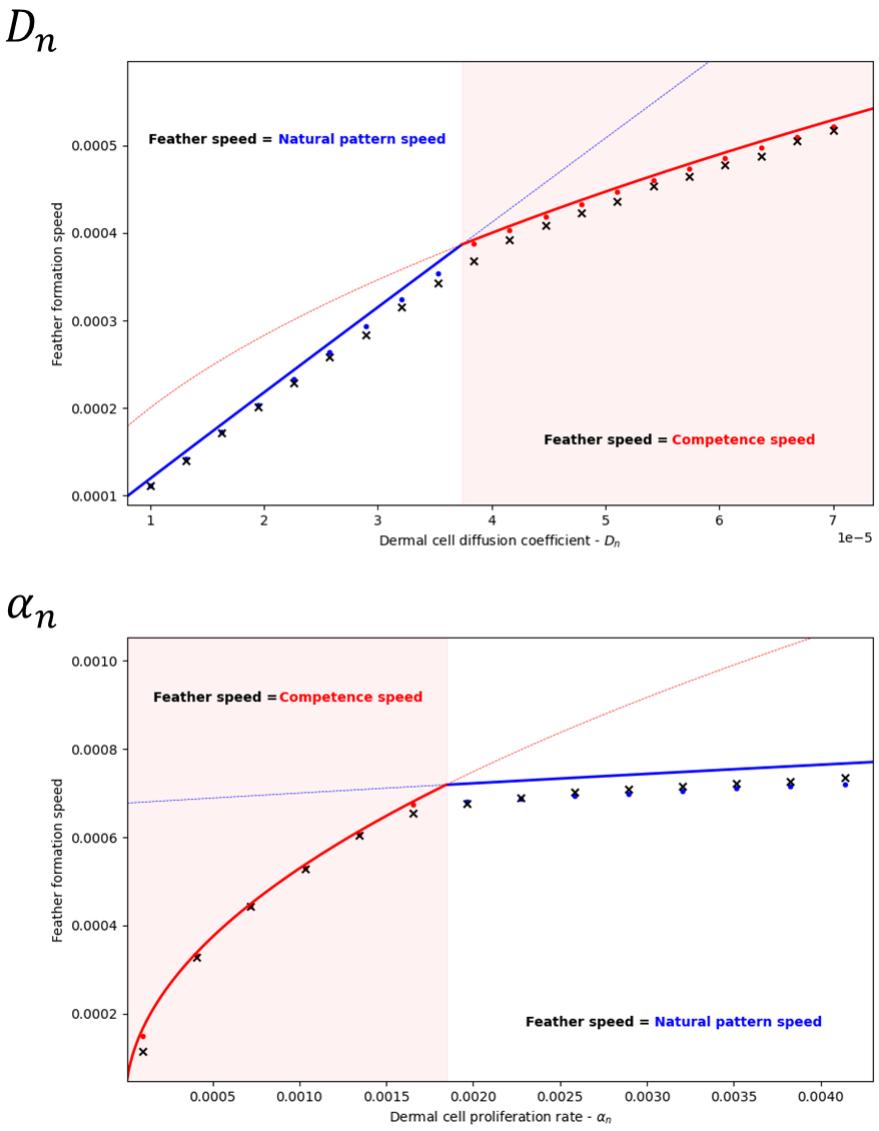

FIGURE 8 – **Speed of emergence of patterns (feather follicles) as a function of D_n and α_n.** The lines represent the influence of the diffusion coefficient D_n (*Top*) and the cell proliferation parameter α_n (*Bottom*) on the natural speed c_{nat} (blue) as well as on the competence speed c_{comp} (red). The black crosses correspond to the estimated emergence speed of patterns from numerical simulations of the system (5). The colored dots represent the values of speeds calculated numerically, with simulation parameter values similar to the black crosses (same time and space discretization), of travelling waves solutions of the Fisher-KPP equation (6) (red) and of the envelope equation (7) (blue). The bold solid lines emphasize the selection principle presented in the equality (8), $c_{\text{pattern}} = \min(c_{\text{comp}}, c_{\text{nat}})$. The values of other parameters are the same as in Figure 2.

the competence wave is faster than the natural speed, it no longer directly impacts the speed of pattern emergence. This is akin to studying pattern emergence within a competent zone. To accomplish this, we opt for a weakly non-linear analysis, which allows us to obtain, under certain conditions, a precise approximation of the envelope. Specifically, it is necessary for the parameter L to be positive (supercritical case) and to be sufficiently close to the critical bifurcation. The envelope equation (7) admits travelling wave solutions that have a critical speed $c_{\text{nat}} = 2\sqrt{\epsilon\nu\sigma}$, denoted as the natural emergence speed of patterns, where ν and σ are defined by the equalities (B.33) and (B.34) while ϵ represents the proximity with respect to the Turing bifurcation. By combining these two possibilities, we derive the speed of feather follicle emergence as given by the following relation $c_{\text{pattern}} \approx \min(2\sqrt{\alpha_n D_n}, 2\epsilon\sqrt{\sigma\nu})$. Although this work is based on modeling feather follicle formation, the theory studied in this article can be adapted to modeling various periodic patterns within other species during embryo development (see, for example, the review [44])

In this article, to determine the speed of follicle formation in the competent zone, we opted for a method based on weakly nonlinear analysis. However, another well-known usable method is based on the marginal stability criterion [45, 46, 47, 48, 49, 50]. Klika, Gaffney, and Maini demonstrated in [30] that, for a system of two reaction-diffusion equations, the application of this method, close to a supercritical bifurcation, predicts the same propagation speed as the weakly nonlinear analysis. However, this marginal stability method does not provide any information about the pattern amplitude or the transient profile of the wave.

Other aspects of the problem can be considered in subsequent works. A first direction we are going to would involve extending the present analysis to the two dimensional setting. When the domain is two dimensional new phenomena appear, such as rhombi, hexagons or mixed-mode patterns ; which can also be predicted by the weakly nonlinear analysis [28, 51, 52, 53, 54].

Another direction of improvement would be to consider the notion of modulated front. A modulated front solution is a front connecting an unstable homogeneous stationary state to a spatially periodic pattern. The first known results of the existence of modulated traveling waves come from the articles of Eckmann, Collet and Wayne [55, 56, 57]. Initially they showed the existence of modulated fronts for the Swift-Hohenberg equation with cubic nonlinearity. Subsequently, many results improved this theory and several models were treated, such as the existence of modulated front for a non-local Fisher equation KPP in the article [58]. Similarly, the theory of a "triggered/quenched front" combining a pattern-forming front with a wave of external competence developed notably by Ryan Goh & Arnd Scheel, could be a useful tool [59, 60, 61, 62, 63].

Acknowledgement

The authors were funded by the ANR via the project PLUME under grant agreement ANR-21-CE13-0040.

A Additional information on linear analysis

In this section we shall investigate, for the system (5), the possibility of pattern emergence with a linear stability analysis. We will show that the point equilibirum $(1, u_s, v_s)$ can be stable for the kinetic part of the system (5), but unstable for the full reaction-diffusion system.

The linearized system in the neighborhood of $(1, u_s, v_s)$ is :

$$\mathbf{w}_t = J\mathbf{w} + D^\kappa \nabla^2 \mathbf{w}, \quad \text{with } \mathbf{w} \equiv \begin{pmatrix} n-1 \\ u-u_s \\ v-v_s \end{pmatrix}, \tag{A.22}$$

where J and D^κ are given by

$$J := \begin{pmatrix} -\alpha_n & 0 & 0 \\ \delta_u u_s & \gamma_u - \delta_u & -\gamma_v \\ \delta_v v_s & \eta_u & -\delta_v \end{pmatrix}, \quad D^\kappa := \begin{pmatrix} D_n & -\kappa & 0 \\ 0 & D_u & 0 \\ 0 & 0 & D_v \end{pmatrix}.$$

The solution of (A.22) with the form $\mathbf{w} = \overline{\mathbf{w}} e^{ikx+\lambda t}$ leads to the following dispersion relation, which characterizes the relation between eigenvalue λ and the wavenumber k

$$0 = \lambda^3 + a_2(k^2)\lambda^2 + a_1(k^2)\lambda + a_0(k^2), \tag{A.23}$$

where

$$a_2(k^2) = \delta_u - \gamma_u + k^2 D_u + \delta_v + k^2 D_v + \alpha_n + k^2 D_n,$$
$$a_1(k^2) = (\alpha_n + k^2 D_n)\left[\delta_u - \gamma_u + k^2 D_u + \delta_v + k^2 D_v\right] + \left[\gamma_v \eta_u + (\gamma_u - \delta_u - k^2 D_u)(-\delta_v - k^2 D_v)\right] - k^2 \kappa \delta_u u_s,$$

and $a_0(k^2) = -\det(A(k^2))$, where $A(k^2) := J - k^2 D$. The Routh-Hurwitz criterion provides three conditions for ensuring that the equilibrium is stable (i.e. eigenvalues have strictly negative real part). In detail, all eigenvalues have strictly negative real part if and only if these conditions hold

$$a_0(k^2) > 0,\ a_2(k^2) > 0 \quad \text{and} \quad a_2(k^2)a_1(k^2) - a_0(k^2) > 0. \tag{A.24}$$

Turing instability emerges when the real parts of two eigenvalues remain negative and the remaining one eigenvalue passes through zero. Without any loss of generality, we assume that λ_1, λ_2 and λ_3 represent the roots of the characteristic equation, and accordingly, we obtain

$$\lambda_1 + \lambda_2 + \lambda_3 = -a_2(k^2), \quad \lambda_1\lambda_2 + \lambda_2\lambda_3 + \lambda_3\lambda_1 = a_1(k^2), \quad \lambda_1\lambda_2\lambda_3 = -a_0(k^2),$$

$$\text{and,} \quad -(\lambda_1 + \lambda_2)(\lambda_2 + \lambda_3)(\lambda_3 + \lambda_1) = a_2(k)a_1(k^2) - a_0(k^2).$$

We assume that there is a Turing instability and k_c denotes the critical wavenumber. Thus, at this critical wavenumber $k = k_c$, we can assumme without any loss of generality

$$\lambda_1|_{k^2=k_c^2} = 0, \quad \text{Re}\,(\lambda_2)|_{k^2=k_c^2} < 0, \text{ and Re}\,(\lambda_3)|_{k^2=k_c^2} < 0.$$

Hence, we have $a_0(k^2) = 0$ at the critical wavenumber $k = k_c$.

Moreover, the conditions for Turing instability leads to $a_2(k_c^2) > 0$, $a_1(k_c^2) = \lambda_2\lambda_3 > 0$ and $a_2(k_c^2)a_1(k_c^2) - a_0(k_c^2) = a_1(k_c^2)a_2(k_c^2) > 0$. Thus, the point equilibrium $(1, u_s, v_s)$ becomes Turing unstable when $\det(A(k^2)) > 0$ holds for at least one $k > 0$ and it remains stable when $\det(A(k^2)) < 0$ holds for all $k \geq 0$.

The determinant of the matrix $A(k^2)$ has the following form

$$\det(A(k^2)) = k^6 A_6 + k^4 A_4(\kappa) + k^2 A_2(\kappa) + A_0,$$

with

$$\begin{aligned}
A_6 &= -D_n D_u D_v < 0,\\
A_4(\kappa) &= -\alpha_n D_u D_v - D_n D_u \delta_v + D_n D_v(\gamma_u - \delta_u) + \kappa \delta_u u_s D_v,\\
A_2(\kappa) &= \alpha_n \left(D_v(\gamma_u - \delta_u) - D_u \delta_v\right) - D_n \left(\gamma_v \eta_u - \delta_v(\gamma_u - \delta_u)\right) - \kappa \left[\gamma_v \delta_v v_s - \delta_u u_s \delta_v\right],\\
A_0 &= -\alpha_n \left[\gamma_v \eta_u - \delta_v(\gamma_u - \delta_u)\right].
\end{aligned}$$

The condition for the marginal stability at some $k = k_c$ is

$$\max\left[\det\left(A(k_c^2)\right)\right] = 0.$$

The minimum of a_0 is attained when

$$k_{\max}^2(\kappa) = \frac{A_4(\kappa) + \sqrt{A_4(\kappa)^2 + 3A_2(\kappa)|A_6|}}{3|A_6|},$$

which requires $A_4(\kappa)^2 + 3A_2(\kappa)|A_0| > 0$ and $A_4(\kappa) + \sqrt{A_4(\kappa)^2 + 3A_2(\kappa)|A_6|} > 0$. As shown in Fig. 9, the graph of $a_0(k)$ depends on κ, which plays the role of the bifurcation parameter. Bifurcation can occur at the critical value, κ_c defined by the root of the function,

$$\kappa \longmapsto k_{\max}^6(\kappa)A_6 + k_{\max}^4(\kappa)A_4(\kappa) + k_{\max}^2(\kappa)A_2(\kappa) + A_0,$$

and k_c is given by $k_c^2 := k_{\max}^2(\kappa_c)$. This function does not necessarily admit a unique root, when it does, the root is approximated numerically. In the case $\kappa < \kappa_c$, the equilibrium point $(1, u_s, v_s)$ is stable for all k (See Fig. 9) While, for $\kappa > \kappa_c$ the system admits a pattern-forming stationary instability. The unstable wavenumbers stay in between the roots of $a_0(k)$, denoted by k_1 and k_2 (See Fig. 9).

B Additional information on weakly nonlinear analysis

In this section, we detail the application of weakly nonlinear analysis to the model (5). We begin by explicitly providing the definitions of the operators $(\mathcal{L}^i)$ and $(\mathcal{B}^i)$ for $i = 0, 1, 2$, introduced in the equations (12) and (13),

$$\mathcal{L}^0(\mathbf{w}) := (J + D^{\kappa_c}\partial_{xx})\mathbf{w}, \qquad \mathcal{L}^1(\mathbf{w}) := 2D^{\kappa_c}\partial_{xX}\mathbf{w} - M_{\kappa_1}\partial_{xx}\mathbf{w},$$

$$\mathcal{L}^2(\mathbf{w}) := D^{\kappa_c}\partial_{XX}\mathbf{w} - M_{\kappa_2}\partial_{xx}\mathbf{w} - 2M_{\kappa_1}\partial_{xX}\mathbf{w}, \qquad \text{with } M_{\kappa_i} := \begin{pmatrix} 0 & \kappa_i & 0\\ 0 & 0 & 0\\ 0 & 0 & 0 \end{pmatrix},$$

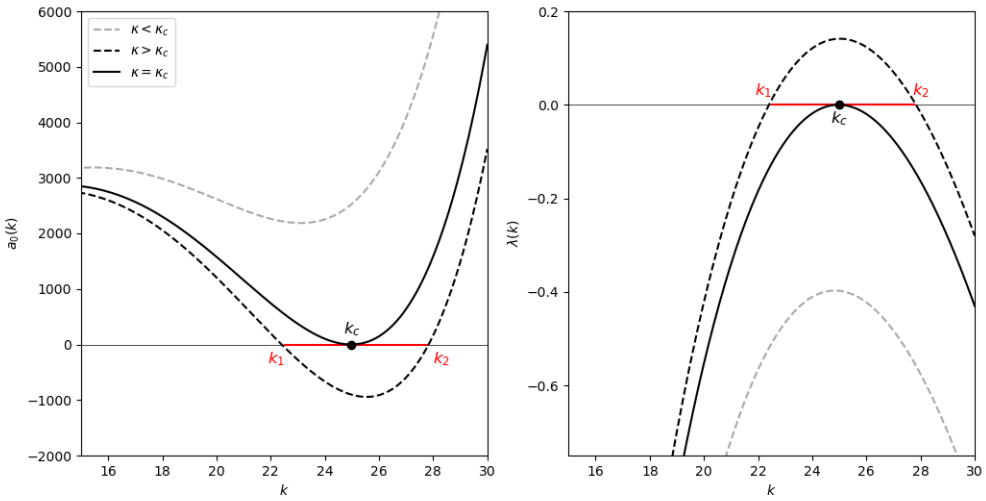

FIGURE 9 – *Left* : Plot of $a_0(k)$. *Right* : Growth rate of the kth mode, with a band of growing modes.

$$\mathcal{B}^0(\mathbf{w},\mathbf{w}') := \frac{1}{2}\begin{pmatrix} -2\alpha_n n' n \\ \gamma_u(n'u + nu') - \gamma_v(n'v + nv') \\ \eta_u(n'u + un') \end{pmatrix} - \frac{\kappa_c}{2}\begin{pmatrix} \partial_x(n'\partial_x u + n\partial_x u') \\ 0 \\ 0 \end{pmatrix},$$

and

$$\mathcal{B}^i(\mathbf{w},\mathbf{w}') := -\frac{\kappa_i}{2}\begin{pmatrix} \partial_x(n'\partial_x u + n\partial_x u') \\ 0 \\ 0 \end{pmatrix}, \qquad \text{for } i = 1, 2.$$

The vector ρ, introduced in the equality (17), is defined up to a constant and can be normalized in the following way

$$\rho = \begin{pmatrix} 1 \\ M_y \\ M_z \end{pmatrix} \in \ker(K - k_c^2 D^{\kappa_c}), \tag{B.25}$$

with

$$M_y = \frac{\alpha_n + k_c^2 D_n}{k_c^2 \kappa_c}, \qquad M_z = \frac{\delta_u u_s + M_y[\gamma_u - \delta_u - k_c^2 D_u]}{\gamma_v}.$$

The equations (15), and (16) can be rewritten in the following form

$O(\epsilon^2)$:

$$\mathcal{L}^0(\mathbf{w}_2) = \mathbf{F}, \tag{B.26}$$

$O(\epsilon^3)$:

$$\mathcal{L}^0(\mathbf{w}_3) = \mathbf{G}, \tag{B.27}$$

with

$$\mathbf{F} =: \partial_{T_1}\mathbf{w}_1 - \mathcal{L}^1(\mathbf{w}_1) - \mathcal{B}^0(\mathbf{w}_1, \mathbf{w}_1), \tag{B.28}$$

and

$$\mathbf{G} =: \partial_{T_2}\mathbf{w}_1 + \partial_{T_1}\mathbf{w}_2 - \mathcal{L}^1(\mathbf{w}_2) - \mathcal{L}^2(\mathbf{w}_1) - \mathcal{B}^1(\mathbf{w}_1, \mathbf{w}_1) - 2\mathcal{B}^0(\mathbf{w}_1, \mathbf{w}_2). \tag{B.29}$$

Substituting (17) into (B.28) leads to

$$\begin{aligned}\mathbf{F} = \cos(k_c x)\rho\left[\frac{\partial A}{\partial T_1} - k_c^2 A M_{\kappa_1}\right] + 2k_c D^{\kappa_c}\rho\frac{\partial A}{\partial X}\sin(k_c x) \\ - \frac{A^2\cos(2k_c x)}{2}\begin{pmatrix} 2\kappa_c k_c^2 M_y - \alpha_n \\ \gamma_u M_y - \gamma_v M_z \\ \eta_u M_y \end{pmatrix} - \frac{A^2}{2}\begin{pmatrix} -\alpha_n \\ \gamma_u M_y - \gamma_v M_z \\ \eta_u M_y \end{pmatrix}.\end{aligned}$$

By the Fredholm alternative, Eq. (B.26) admits solution if and only if

$$\langle \mathbf{F}, \mathbf{W}^\star \rangle = 0, \tag{B.30}$$

where $\mathbf{W}^\star = \psi\cos(k_c x) \in \ker(L^\star)$ with $L^\star$ the adjoint operator of $\mathcal{L}^0$ and $\langle\cdot,\cdot\rangle$ is the scalar product in $L^2(0, 2\pi/k_c)$. Due to the Neumann boundary condition, for (5) we can construct a solution in the whole domain using reflection and periodic extension. The vector ψ is defined up to a constant,

$$\psi := \begin{pmatrix} 1 \\ M_y^\star \\ M_z^\star \end{pmatrix}, \text{ with } M_y^\star = -M_z^\star\frac{\delta_v + k_c^2 D_v}{\gamma_v},\ M_z^\star = \frac{\gamma_v k_c^2 \kappa_c}{(\delta_v + k_c^2 D_v)(\gamma_u - \delta_u - k_c^2 D_u) - \eta_u\gamma_v}.$$

The condition (B.30) gives us

$$\partial_{T_1} A = \gamma A, \quad \gamma = \frac{k_c^2\kappa_1 M_y}{1 + M_y M_y^\star + M_z M_z^\star}. \tag{B.31}$$

Obviously, the above equation cannot correctly predict the evolution of amplitude. Thus, we take $T_1 = 0$ and $\kappa_1 = 0$ such that the solvability condition (B.30) holds. Therefore the solution of (B.26) with the boundary condition has the following form

$$\mathbf{w}_2 = A^2\mathbf{w}_{20} + A^2\mathbf{w}_{22}\cos(2k_c x) + \frac{\partial A}{\partial X}\mathbf{w}_{21}\sin(k_c x),$$

where vectors $\mathbf{w}_{2i}$, $i = 0, 1, 2$, are the solutions of the following linear systems :

$$\begin{cases} J\mathbf{w}_{20} = \dfrac{1}{2}\begin{pmatrix} -\alpha_n \\ \gamma_u M_y - \gamma_v M_z \\ \eta_u M_y \end{pmatrix}, \\ (J - k_c^2 D^{\kappa_c})\mathbf{w}_{21} = 2k_c D^{\chi_c}\rho, \\ (J - 4k_c^2 D^{\kappa_c})\mathbf{w}_{22} = -\dfrac{1}{2}\begin{pmatrix} 2\kappa_c k_c^2 M_y - \alpha_n \\ \gamma_u M_y - \gamma_v M_z \\ \eta_u M_y \end{pmatrix}. \end{cases} \tag{B.32}$$

To understand the evolution of the amplitude A we must consider the third order coefficient equation (B.27). The solvability condition $\langle \mathbf{G}, \mathbf{W}^\star \rangle = 0$ leads to this following equation for the amplitude A,

$$\partial_{T_2} A = \nu \partial_{XX} A + \sigma A - L A^3,$$

where the parameters ν, σ and L are given by

$$\nu := \frac{\langle 2k_c D^{\kappa_c} \mathbf{w}_{21} + D^{\kappa_c} \rho, \psi \rangle}{\langle \rho, \psi \rangle}, \tag{B.33}$$

$$\sigma := \frac{\langle \mathbf{G}_{11}, \psi \rangle}{\langle \rho, \psi \rangle}, \tag{B.34}$$

$$L := \frac{\langle \mathbf{G}_{13}, \psi \rangle}{\langle \rho, \psi \rangle}, \tag{B.35}$$

with

$$\mathbf{G}_{11} = -k_c^2 M_{\kappa_2} \rho, \quad \text{and} \quad \mathbf{G}_{13} := -\kappa_c k_c^2 \begin{pmatrix} M_y W_{20}^{(1)} + W_{22}^{(2)} - \dfrac{M_y}{2} W_{22}^{(1)} \\ 0 \\ 0 \end{pmatrix} - \mathbf{V}_{20} - \mathbf{V}_{22},$$

where $W_{2j}^{(i)}$ corresponds to the i-th component of $\mathbf{w}_{2j}$. The two vectors $\mathbf{V}_{20}$ and $\mathbf{V}_{22}$ are defined by

$$\mathbf{V}_{20} := \begin{pmatrix} -2\alpha_n W_{20}^{(1)} \\ \gamma_u \left[W_{20}^{(2)} + M_y W_{20}^{(1)} \right] - \gamma_v \left[W_{20}^{(1)} M_z + W_{20}^{(3)} \right] \\ \eta_u \left[W_{20}^{(2)} + M_y W_{20}^{(1)} \right] \end{pmatrix},$$

$$\mathbf{V}_{22} := \frac{1}{2} \begin{pmatrix} -2\alpha_n W_{22}^{(1)} \\ \gamma_u \left[W_{22}^{(2)} + M_y W_{22}^{(1)} \right] - \gamma_v \left[W_{22}^{(1)} M_z + W_{22}^{(3)} \right] \\ \eta_u \left[W_{22}^{(2)} + M_y W_{22}^{(1)} \right] \end{pmatrix}.$$

C Supplementary Figures

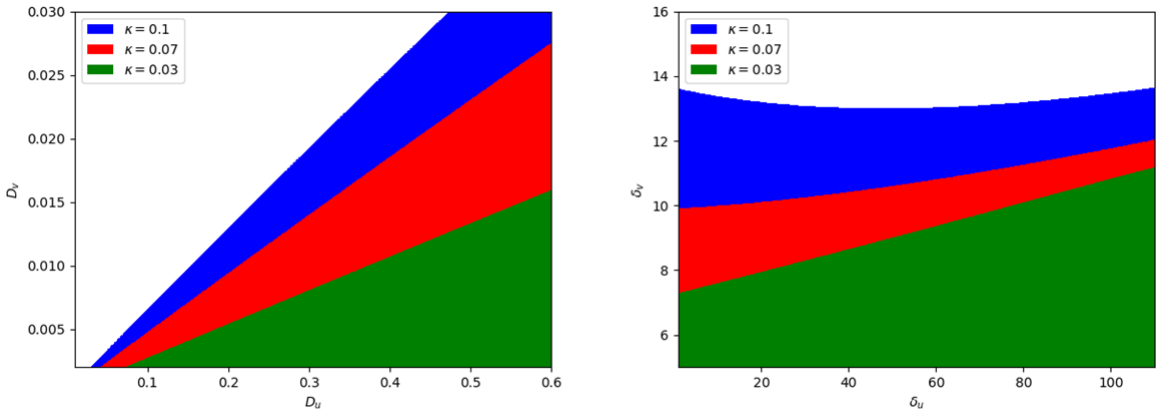

FIGURE 10 – The colored areas correspond to parameter values for which the point $(1, u_s, v_s)$ admits a Turing-type instability. The different colors correspond to different chemotaxis parameters 0.1, 0.07 and 0.03. In the left figure, the parameters studied are the pair of diffusion coefficients (D_u, D_v) and on the right figure, the parameters studied are the pair of degradation coefficients (δ_u, δ_v).

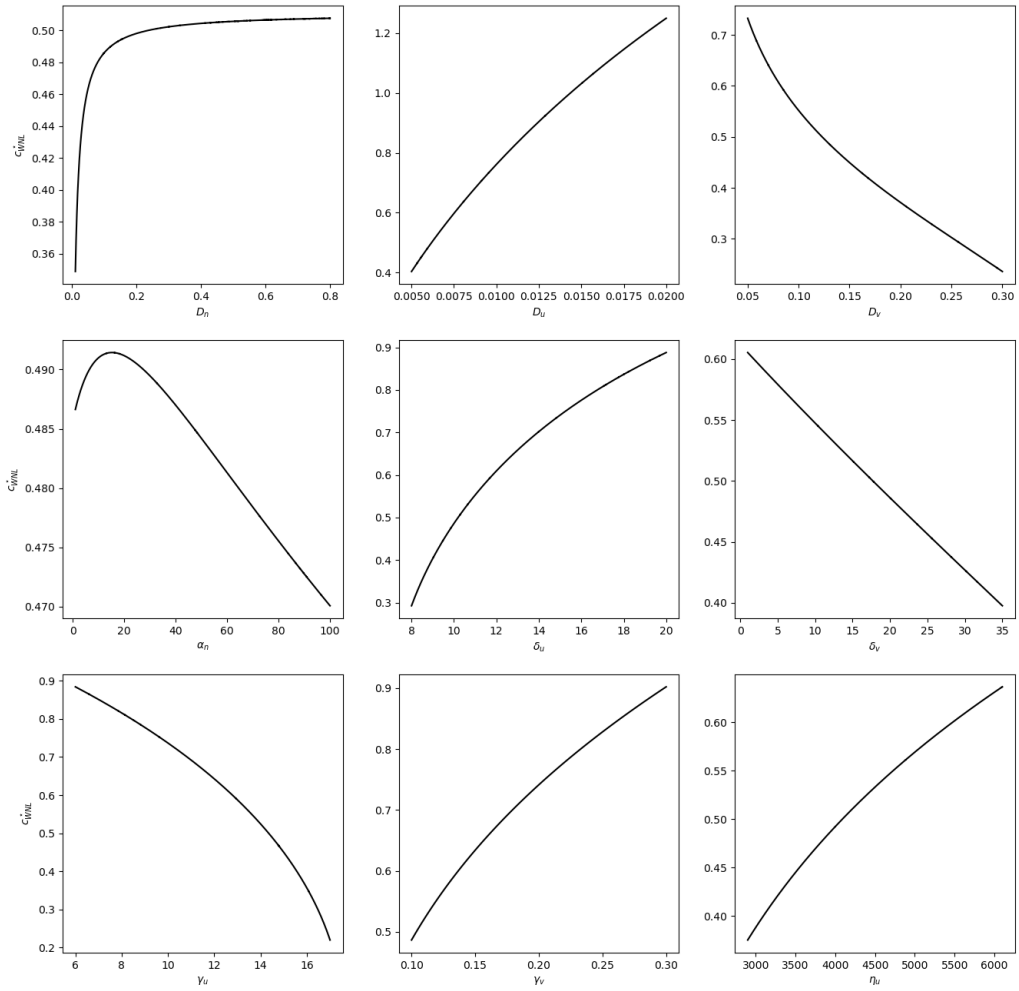

FIGURE 11 – **Influence of the parameter values on the critical speed $c^\star_{\mathbf{WNL}}$ of the equation** (7)**.** For each sub figure we change only one parameter, the values of the other parameters are the same as in Figure 2. For each parameter value we calculate again the critical bifurcation value.

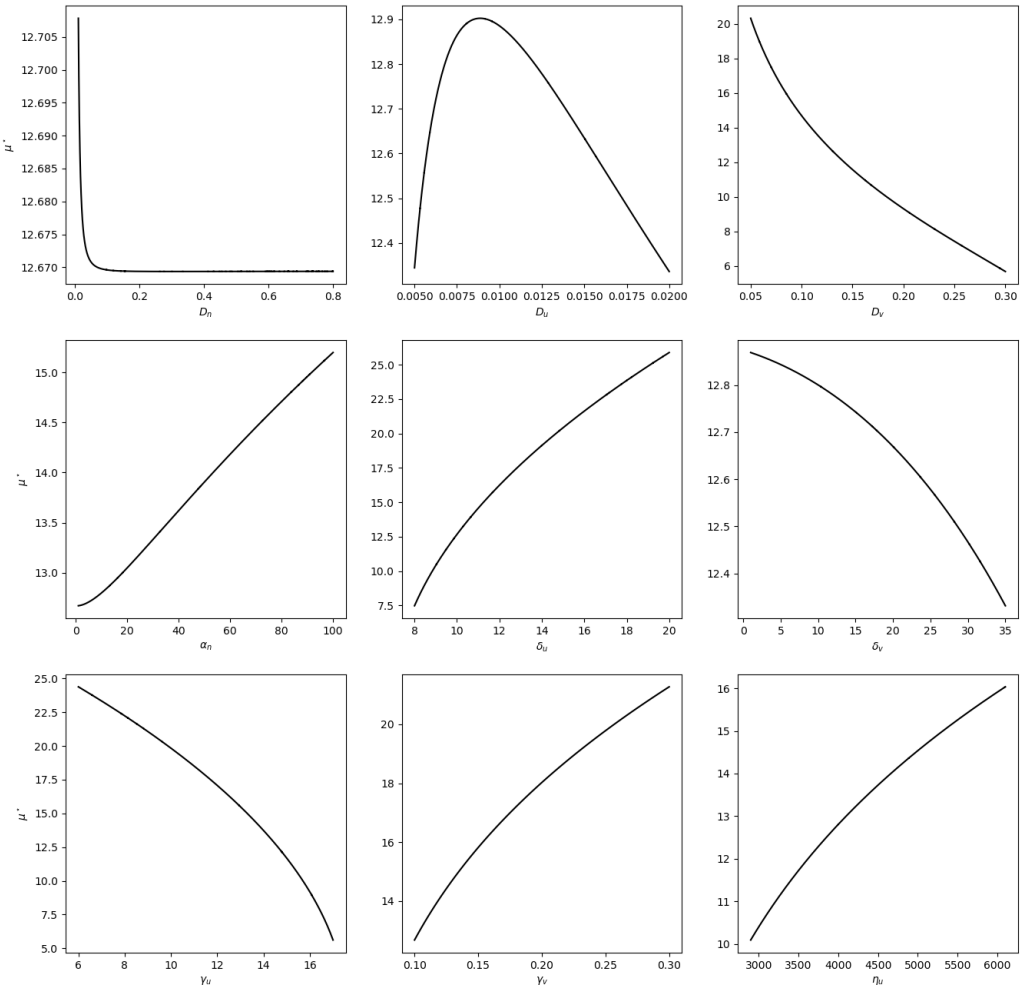

FIGURE 12 – **Influence of the parameter values on the steepness $\mu^\star$ of the equation (7) at the critical speed.** For each sub figure we change only one parameter, the values of the other parameters are the same as in Figure 2. For each parameter value we calculate again the critical bifurcation value.

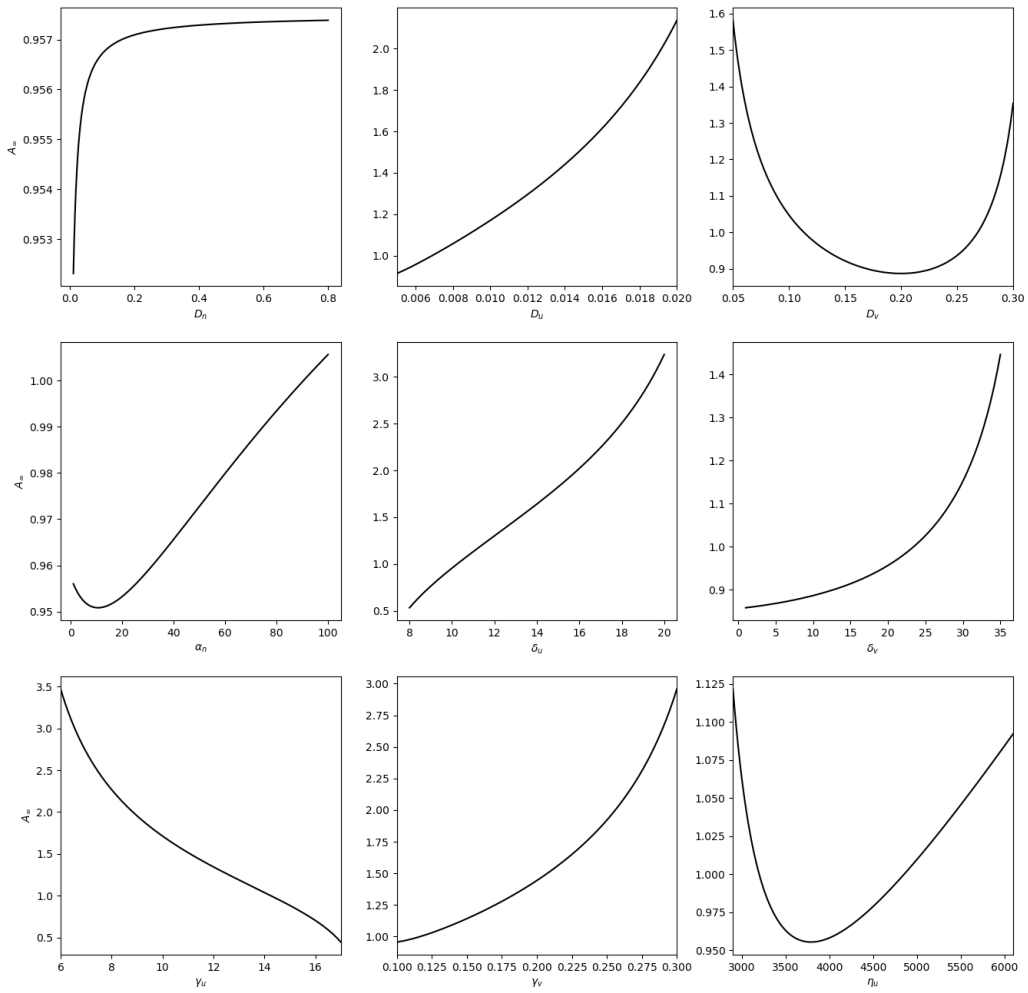

FIGURE 13 – **Influence of the parameter values on the final amplitude of the patterns, A_∞, of the equation** (7)**.** For each sub figure we change only one parameter, the values of the other parameters are the same as in Figure 2. For each parameter value we calculate again the critical bifurcation value.

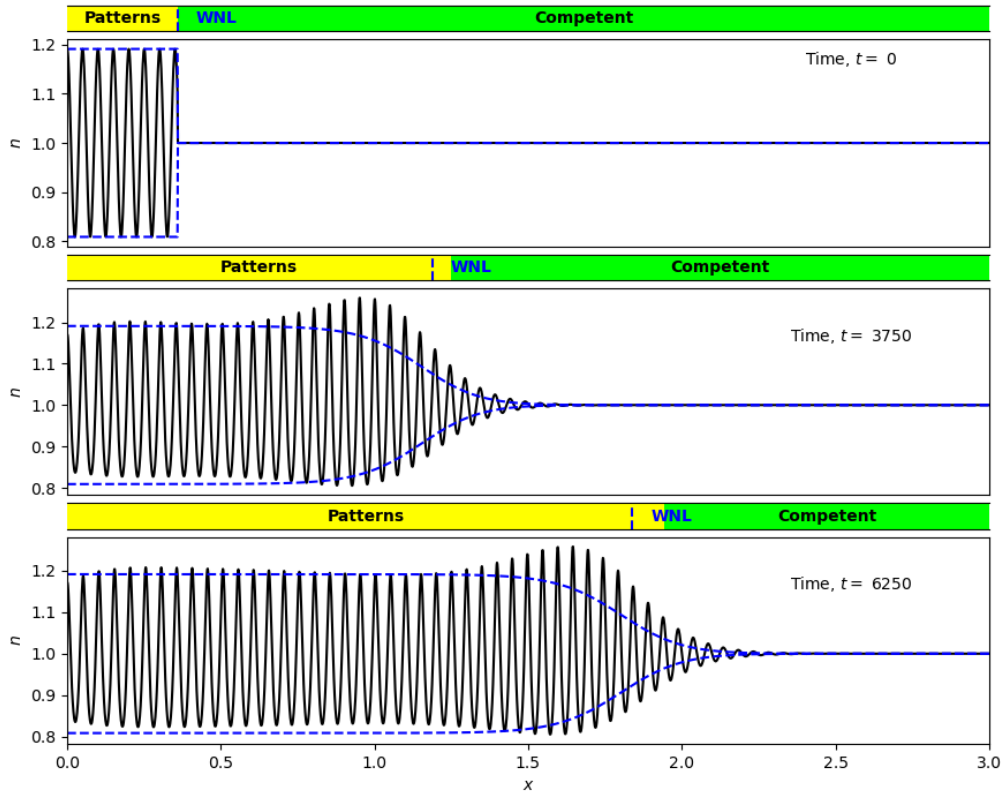

FIGURE 14 – **Comparison between the solution of the equation** (7) **(blue dashed line) and the numerical solution of** (5) **(black solid line) at different times.** The panels above the figures respectively represent the competent zone (green), the zone where patterns are present (yellow), and the prediction of the weakly nonlinear analysis (blue dashed line). Parameter values are the same as in the previous figure 3 except for $\epsilon = 0.2$.

References

[1] A. M. Turing. « The chemical basis of morphogenesis ». en. In : *Bulletin of Mathematical Biology* 52.1-2 (jan. 1990), p. 153-197. doi : 10.1007/BF02459572. url : http://link.springer.com/10.1007/BF02459572.

[2] Kevin J. Painter, Mariya Ptashnyk et Denis J. Headon. « Systems for intricate patterning of the vertebrate anatomy ». en. In : *Philosophical Transactions of the Royal Society A : Mathematical, Physical and Engineering Sciences* 379.2213 (déc. 2021), p. 20200270. doi : 10.1098/rsta.2020.0270. url : https://royalsocietypublishing.org/doi/10.1098/rsta.2020.0270.

[3] Alexa Sadier et al. « Modeling Edar expression reveals the hidden dynamics of tooth signaling center patterning ». en. In : *PLOS Biology* 17.2 (fév. 2019). Sous la dir. de Caroline S. Hill, e3000064. doi : 10.1371/journal.pbio.3000064. url : https://dx.plos.org/10.1371/journal.pbio.3000064.

[4] Chunyan Mou et al. « Generation of the primary hair follicle pattern ». en. In : *Proceedings of the National Academy of Sciences* 103.24 (juin 2006), p. 9075-9080. doi : 10.1073/pnas.0600825103. url : https://pnas.org/doi/full/10.1073/pnas.0600825103.

[5] James D. Glover et al. « Hierarchical patterning modes orchestrate hair follicle morphogenesis ». en. In : *PLOS Biology* 15.7 (juill. 2017). Sous la dir. de Caroline Hill, e2002117. doi : 10.1371/journal.pbio.2002117. url : https://dx.plos.org/10.1371/journal.pbio.2002117.

[6] P.M. Kulesa et al. « On a Model Mechanism for the Spatial Patterning of Teeth Primordia in the Alligator ». en. In : *Journal of Theoretical Biology* 180.4 (juin 1996), p. 287-296. doi : 10.1006/jtbi.1996.0103. url : https://linkinghub.elsevier.com/retrieve/pii/S0022519396901034.

[7] William K. W. Ho et al. « Feather arrays are patterned by interacting signalling and cell density waves ». en. In : *PLOS Biology* 17.2 (fév. 2019). Sous la dir. de Gregory S. Barsh, e3000132. doi : 10.1371/journal.pbio.3000132. url : https://dx.plos.org/10.1371/journal.pbio.3000132.

[8] Rory L. Cooper et al. « An ancient Turing-like patterning mechanism regulates skin denticle development in sharks ». en. In : *Science Advances* 4.11 (nov. 2018), eaau5484. doi : 10.1126/sciadv.aau5484. url : https://www.science.org/doi/10.1126/sciadv.aau5484.

[9] Maya N. Evanitsky et Stefano Di Talia. « An active traveling wave of Eda/NF-kappaB signaling controls the timing and hexagonal pattern of skin appendages in zebrafish ». en. In : *Development* 150.18 (sept. 2023), dev201866. doi : 10.1242/dev.201866. url : https://journals.biologists.com/dev/article/150/18/dev201866/329117/An-active-traveling-wave-of-Eda-NF-B-signaling.

[10] Alexa Sadier et al. « Bat teeth illuminate the diversification of mammalian tooth classes ». en. In : *Nature Communications* 14.1 (août 2023), p. 4687. doi : 10.1038/s41467-023-40158-4. url : https://www.nature.com/articles/s41467-023-40158-4.

[11] Richard Bailleul et al. « Symmetry breaking in the embryonic skin triggers directional and sequential plumage patterning ». en. In : *PLOS Biology* 17.10 (oct. 2019). Sous la dir. de Caroline S. Hill, e3000448. doi : 10.1371/journal.pbio.3000448. url : https://dx.plos.org/10.1371/journal.pbio.3000448.

[12] Athanasia C. Tzika et al. « Somitic positional information guides self-organized patterning of snake scales ». en. In : *Science Advances* 9.24 (juin 2023), eadf8834. doi : 10.1126/sciadv.adf8834. url : https://www.science.org/doi/10.1126/sciadv.adf8834.

[13] Danielle Dhouailly. « A new scenario for the evolutionary origin of hair, feather, and avian scales ». en. In : *Journal of Anatomy* 214.4 (avr. 2009), p. 587-606. doi : 10.1111/j.1469-7580.2008.01041.x. url : https://onlinelibrary.wiley.com/doi/10.1111/j.1469-7580.2008.01041.x.

[14] Antoine Diez et al. « Turing Pattern Formation in Reaction-Cross-Diffusion Systems with a Bilayer Geometry ». en. In : *Bulletin of Mathematical Biology* 86.2 (fév. 2024), p. 13. doi : 10.1007/s11538-023-01237-1. url : https://link.springer.com/10.1007/s11538-023-01237-1.

[15] Chun-Chih Tseng et al. « Gap junctions in Turing-type periodic feather pattern formation ». en. In : *PLOS Biology* 22.5 (mai 2024). Sous la dir. de Gregory S. Barsh, e3002636. doi : 10.1371/journal.pbio.3002636. url : https://dx.plos.org/10.1371/journal.pbio.3002636.

[16] Frederic Michon et al. « BMP2 and BMP7 play antagonistic roles in feather induction ». en. In : *Development* 135.16 (août 2008), p. 2797-2805. doi : 10.1242/dev.018341. url : https://journals.biologists.com/dev/article/135/16/2797/43645/BMP2-and-BMP7-play-antagonistic-roles-in-feather.

[17] Kevin J. Painter, William Ho et Denis J. Headon. « A chemotaxis model of feather primordia pattern formation during avian development ». en. In : *Journal of Theoretical Biology* 437 (jan. 2018), p. 225-238. doi : 10.1016/j.jtbi.2017.10.026. url : https://linkinghub.elsevier.com/retrieve/pii/S0022519317304952.

[18] Nicolás A. Barnafi et al. « Coupling Chemotaxis and Growth Poromechanics for the Modelling of Feather Primordia Patterning ». en. In : *Mathematics* 10.21 (nov. 2022), p. 4096. doi : 10.3390/math10214096. url : https://www.mdpi.com/2227-7390/10/21/4096.

[19] Akiko Nakamasu et al. « Interactions between zebrafish pigment cells responsible for the generation of Turing patterns ». en. In : *Proceedings of the National Academy of Sciences* 106.21 (mai 2009), p. 8429-8434. doi : 10.1073/pnas.0808622106. url : https://pnas.org/doi/full/10.1073/pnas.0808622106.

[20] Liana Manukyan et al. « A living mesoscopic cellular automaton made of skin scales ». en. In : *Nature* 544.7649 (avr. 2017), p. 173-179. doi : 10.1038/nature22031. url : https://www.nature.com/articles/nature22031.

[21] Ebrahim Jahanbakhsh et Michel C. Milinkovitch. « Modeling convergent scale-by-scale skin color patterning in multiple species of lizards ». en. In : *Current Biology* 32.23 (déc. 2022), 5069-5082.e13. doi : 10.1016/j.cub.2022.10.044. url : https://linkinghub.elsevier.com/retrieve/pii/S096098222201692X.

[22] Andrew D. Economou, Nicholas A. M. Monk et Jeremy B. A. Green. « Perturbation analysis of a multi-morphogen turing reaction-diffusion stripe patterning system reveals key regulatory interactions ». en. In : *Development* (jan. 2020), dev.190553. doi : 10.1242/dev.190553. url : https://journals.biologists.com/dev/article/doi/10.1242/dev.190553/267065/Perturbation-analysis-of-a-multi-morphogen-turing.

[23] Jiashan Zheng et al. « A new result for global existence and boundedness of solutions to a parabolic–parabolic Keller–Segel system with logistic source ». en. In : *Journal of Mathematical Analysis and Applications* 462.1 (juin 2018), p. 1-25. doi : 10.1016/j.jmaa.2018.01.064. url : https://linkinghub.elsevier.com/retrieve/pii/S0022247X18301021.

[24] Yue Liu, Philip K Maini et Ruth E Baker. « Control of diffusion-driven pattern formation behind a wave of competency ». In : *Physica D : Nonlinear Phenomena* (2022). Publisher : Elsevier, p. 133297.

[25] R. A. Fisher. « The wave of advance of advantageous genes ». en. In : *Annals of Eugenics* 7.4 (juin 1937), p. 355-369. doi : 10.1111/j.1469-1809.1937.tb02153.x. url : https://onlinelibrary.wiley.com/doi/10.1111/j.1469-1809.1937.tb02153.x.

[26] Andrei Nikolaevitch Kolmogorov. « A study of the equation of diffusion with increase in the quantity of matter, and its application to a biological problem ». In : *Moscow University Bulletin of Mathematics* 1 (1937), p. 1-25.

[27] G. Gambino, M.C. Lombardo et M. Sammartino. « Turing instability and traveling fronts for a nonlinear reaction–diffusion system with cross-diffusion ». en. In : *Mathematics and Computers in Simulation* 82.6 (fév. 2012), p. 1112-1132. doi : 10.1016/j.matcom.2011.11.004. url : https://linkinghub.elsevier.com/retrieve/pii/S0378475411002692.

[28] B. Bozzini et al. « Weakly nonlinear analysis of Turing patterns in a morphochemical model for metal growth ». en. In : *Computers & Mathematics with Applications* 70.8 (oct. 2015), p. 1948-1969. doi : 10.1016/j.camwa.2015.08.019. url : https://linkinghub.elsevier.com/retrieve/pii/S0898122115003880.

[29] Manjun Ma et al. « Chemotaxis-driven pattern formation for a reaction–diffusion–chemotaxis model with volume-filling effect ». en. In : *Computers & Mathematics with Applications* 72.5 (sept. 2016), p. 1320-1340. doi : 10.1016/j.camwa.2016.06.039. url : https://linkinghub.elsevier.com/retrieve/pii/S0898122116303716.

[30] Václav Klika, Eamonn A. Gaffney et Philip K. Maini. *On the speed of propagation in Turing patterns for reaction-diffusion systems*. en. arXiv :2403.09247 [nlin]. Mars 2024. url : http://arxiv.org/abs/2403.09247.

[31] Camile Fraga Delfino Kunz et al. « Novel Aspects in Pattern Formation Arise from Coupling Turing Reaction–Diffusion and Chemotaxis ». en. In : *Bulletin of Mathematical Biology* 86.1 (jan. 2024), p. 4. DOI : 10.1007/s11538-023-01225-5. URL : https://link.springer.com/10.1007/s11538-023-01225-5.

[32] Camille Curantz et al. « Cell shape anisotropy contributes to self-organized feather pattern fidelity in birds ». en. In : *PLOS Biology* 20.10 (oct. 2022). Sous la dir. de Marianne E. Bronner, e3001807. DOI : 10.1371/journal.pbio.3001807. URL : https://dx.plos.org/10.1371/journal.pbio.3001807.

[33] E. Tulumello, M. C. Lombardo et M. Sammartino. « Cross-Diffusion Driven Instability in a Predator-Prey System with Cross-Diffusion ». en. In : *Acta Applicandae Mathematicae* 132.1 (août 2014), p. 621-633. DOI : 10.1007/s10440-014-9935-7. URL : http://link.springer.com/10.1007/s10440-014-9935-7.

[34] G. Gambino et al. « Turing pattern formation in the Brusselator system with nonlinear diffusion ». en. In : *Physical Review E* 88.4 (oct. 2013), p. 042925. DOI : 10.1103/PhysRevE.88.042925. URL : https://link.aps.org/doi/10.1103/PhysRevE.88.042925.

[35] Valeria Giunta, Maria Carmela Lombardo et Marco Sammartino. « Pattern Formation and Transition to Chaos in a Chemotaxis Model of Acute Inflammation ». en. In : *SIAM Journal on Applied Dynamical Systems* 20.4 (jan. 2021), p. 1844-1881. DOI : 10.1137/20M1358104. URL : https://epubs.siam.org/doi/10.1137/20M1358104.

[36] Renji Han et Binxiang Dai. « Cross-diffusion induced Turing instability and amplitude equation for a toxic-phytoplankton–zooplankton model with nonmonotonic functional response ». In : *International Journal of Bifurcation and Chaos* 27.06 (2017). Publisher : World Scientific, p. 1750088.

[37] Yazhou Han et al. « Wavefront invasion for a volume-filling chemotaxis model with logistic growth ». In : *Computers & Mathematics with Applications* 71.2 (2016). Publisher : Elsevier, p. 471-478.

[38] Yazhou Han et al. « Pattern formation for a volume-filling chemotaxis model with logistic growth ». In : *Journal of Mathematical Analysis and Applications* 448.2 (2017). Publisher : Elsevier, p. 885-907.

[39] K. P. Hadeler et F. Rothe. « Travelling fronts in nonlinear diffusion equations ». en. In : *Journal Of Mathematical Biology* 2.3 (1975), p. 251-263. DOI : 10.1007/BF00277154. URL : http://link.springer.com/10.1007/BF00277154.

[40] Hannes Uecker, Daniel Wetzel et Jens D. M. Rademacher. *pde2path - A Matlab package for continuation and bifurcation in 2D elliptic systems*. en. arXiv :1208.3112 [math]. Sept. 2012. URL : http://arxiv.org/abs/1208.3112.

[41] Hannes Uecker. *Numerical continuation and bifurcation in nonlinear PDEs*. eng. Other Titles 174. Philadelphia : Society for Industrial et Applied Mathematics, 2021.

[42] Hannes Uecker. *Pattern formation with pde2path – a tutorial*. Version Number : 3. 2019. DOI : 10.48550/ARXIV.1908.05211. URL : https://arxiv.org/abs/1908.05211.

[43] W van Saarloos, M van Hecke et PC Hohenberg. « Amplitude equations for pattern forming systems ». In : (1994).

[44] Zoe R. Sudderick et James D. Glover. « Periodic pattern formation during embryonic development ». en. In : *Biochemical Society Transactions* 52.1 (fév. 2024), p. 75-88. doi : 10.1042/BST20230197. url : https://portlandpress.com/biochemsoctrans/article/52/1/75/233994/Periodic-pattern-formation-during-embryonic.

[45] G. Dee et J. S. Langer. « Propagating Pattern Selection ». en. In : *Physical Review Letters* 50.6 (fév. 1983), p. 383-386. doi : 10.1103/PhysRevLett.50.383. url : https://link.aps.org/doi/10.1103/PhysRevLett.50.383.

[46] W Van Saarloos. « Front propagation into unstable states ». en. In : *Physics Reports* 386.2-6 (nov. 2003), p. 29-222. doi : 10.1016/j.physrep.2003.08.001. url : https://linkinghub.elsevier.com/retrieve/pii/S0370157303003223.

[47] Matt Holzer et Arnd Scheel. « Criteria for Pointwise Growth and Their Role in Invasion Processes ». en. In : *Journal of Nonlinear Science* 24.4 (août 2014), p. 661-709. doi : 10.1007/s00332-014-9202-0. url : http://link.springer.com/10.1007/s00332-014-9202-0.

[48] E. Ben-Jacob et al. « Pattern propagation in nonlinear dissipative systems ». en. In : *Physica D : Nonlinear Phenomena* 14.3 (mars 1985), p. 348-364. doi : 10.1016/0167-2789(85)90094-6. url : https://linkinghub.elsevier.com/retrieve/pii/0167278985900946.

[49] Wim Van Saarloos et P.C. Hohenberg. « Fronts, pulses, sources and sinks in generalized complex Ginzburg-Landau equations ». en. In : *Physica D : Nonlinear Phenomena* 56.4 (juin 1992), p. 303-367. doi : 10.1016/0167-2789(92)90175-M. url : https://linkinghub.elsevier.com/retrieve/pii/016727899290175M.

[50] M. R. Myerscough et J. D. Murray. « Analysis of propagating pattern in a chemotaxis system ». en. In : *Bulletin of Mathematical Biology* 54.1 (jan. 1992), p. 77-94. doi : 10.1007/BF02458621. url : http://link.springer.com/10.1007/BF02458621.

[51] G. Gambino, M.C. Lombardo et M. Sammartino. « Pattern formation driven by cross-diffusion in a 2D domain ». en. In : *Nonlinear Analysis : Real World Applications* 14.3 (juin 2013), p. 1755-1779. doi : 10.1016/j.nonrwa.2012.11.009. url : https://linkinghub.elsevier.com/retrieve/pii/S1468121812002593.

[52] Gerhard C Cruywagen, James D Murray et Philip K Maini. « Biological pattern formation on two-dimensional spatial domains : a nonlinear bifurcation analysis ». In : *SIAM Journal on Applied Mathematics* 57.6 (1997). Publisher : SIAM, p. 1485-1509.

[53] Gaetana Gambino et al. « Cross-diffusion effects on stationary pattern formation in the FitzHugh-Nagumo model ». In : *Discrete and Continuous Dynamical Systems - B* 27.12 (2022), p. 7783. doi : 10.3934/dcdsb.2022063. url : https://www.aimsciences.org/article/doi/10.3934/dcdsb.2022063.

[54] Manjun Ma, Meiyan Gao et R. Carretero-González. « Pattern formation for a two-dimensional reaction-diffusion model with chemotaxis ». en. In : *Journal of Mathematical Analysis and Applications* 475.2 (juill. 2019), p. 1883-1909. doi : 10.1016/j.jmaa.2019.03.060. url : https://linkinghub.elsevier.com/retrieve/pii/S0022247X19302811.

[55] P. Collet et J. P. Eckmann. « The existence of dendritic fronts ». en. In : *Communications in Mathematical Physics* 107.1 (mars 1986), p. 39-92. DOI : 10.1007/BF01206953. URL : http://link.springer.com/10.1007/BF01206953.

[56] Pierre Collet et Jean-Pierre Eckmann. *Instabilities and Fronts in Extended Systems :* Princeton University Press, déc. 1990. DOI : 10.1515/9781400861026. URL : https://www.degruyter.com/document/doi/10.1515/9781400861026/html.

[57] J. P. Eckmann et C. E. Wayne. « Propagating fronts and the center manifold theorem ». en. In : *Communications in Mathematical Physics* 136.2 (fév. 1991), p. 285-307. DOI : 10.1007/BF02100026. URL : http://link.springer.com/10.1007/BF02100026.

[58] Grégory Faye et Matt Holzer. « Modulated traveling fronts for a nonlocal Fisher-KPP equation : A dynamical systems approach ». en. In : *Journal of Differential Equations* 258.7 (avr. 2015), p. 2257-2289. DOI : 10.1016/j.jde.2014.12.006. URL : https://linkinghub.elsevier.com/retrieve/pii/S0022039614004653.

[59] Ryan Goh et Arnd Scheel. « Triggered fronts in the complex Ginzburg Landau equation ». In : *Journal of Nonlinear Science* 24.1 (2014). Publisher : Springer, p. 117-144.

[60] Ryan Goh et Arnd Scheel. « Pattern formation in the wake of triggered pushed fronts ». In : *Nonlinearity* 29.8 (2016). Publisher : IOP Publishing, p. 2196.

[61] M. Avery et al. « Growing Stripes, with and without Wrinkles ». en. In : *SIAM Journal on Applied Dynamical Systems* 18.2 (jan. 2019), p. 1078-1117. DOI : 10.1137/18M1221989. URL : https://epubs.siam.org/doi/10.1137/18M1221989.

[62] Ryan Goh et Arnd Scheel. « Pattern-forming fronts in a Swift–Hohenberg equation with directional quenching — parallel and oblique stripes ». en. In : *Journal of the London Mathematical Society* 98.1 (août 2018), p. 104-128. DOI : 10.1112/jlms.12122. URL : https://onlinelibrary.wiley.com/doi/10.1112/jlms.12122.

[63] Ryan Goh et Arnd Scheel. « Growing patterns ». In : *Nonlinearity* 36.10 (oct. 2023), R1-R51. DOI : 10.1088/1361-6544/acf265. URL : https://iopscience.iop.org/article/10.1088/1361-6544/acf265.